



Annual firn pack variations in the context of the climate settings: Example from the Grosser Aletschgletscher using multi-year radar observations

Akash M. Patil^{1,2}, Christoph Mayer², Theo M. Jenk^{3,4}, Astrid Lambrecht², Thorsten Seehaus¹,
Alexander R. Groos¹, and Michelle Worek^{3,4}

¹Institute of Geography, Friedrich-Alexander-Universität Erlangen-Nürnberg, 91508 Erlangen, Germany

²Bavarian Academy of Sciences and Humanities, Geodesy and Glaciology, Alfons-Goppel Str. 11, D-80539 Munich, Germany

³PSI Center for Energy and Environmental Sciences, Paul Scherrer Institute, Villigen, Switzerland

⁴Oeschger Centre for Climate Change Research, University of Bern, Bern, Switzerland

Correspondence: Akash M. Patil (akash.patil@badw.de / akash.patil@fau.de)

Abstract. The glacier mass balance is driven by primary processes such as snowfall and surface melt; secondary processes, like firn pack warming, percolation, and refreezing, are becoming more important even in high-elevation basins, which are triggered by warming Alpine regions. All these processes are functionally related to temporal changes in the firn pack, predominantly its density structure. Here, we provide a detailed assessment of temporal changes in firn density, stratigraphy, and compaction rate at different locations of the glacier accumulation area, representing the first such analysis for a glacier in the European Alps. To achieve this, we combined multi-year geophysical observations, predominantly ground-penetrating radar (GPR)-based common-midpoint (CMP) surveys, with direct firn-core investigations from the accumulation area of the Grosser Aletschgletscher, Switzerland. We estimated temporal changes in firn density and compaction rates within the identified 8-9 annual layers using internal reflection horizons (IRHs) from repeat CMP measurements and analysis of firn core-derived chemical impurity and stable isotope relationship. Our results suggest that the changes in firn density over a year decrease with depth and age, with the largest change ($\sim 130 \text{ kg m}^{-3} \text{ a}^{-1}$) occurring at the near-surface annual layers at a low-lying accumulation area where the summer surface melt is more significant than at the higher elevations. Similarly, the estimated compaction rate (maximum $\sim 0.3 \text{ m a}^{-1}$ near the surface) decreases with depth and age. The CMP-derived density–depth profile agrees with the firn-core results, demonstrating that CMP measurements are a valuable alternative for increasing the spatial distribution of observations and complementing invasive, labour-intensive glaciological measurements. We also estimated spatial changes in firn density and accumulation along a GPR transect and traced the spatial extent of the firn body. The comparison of GPR observations from winter 2024 and 2025 reveals a potential effect of glacier dynamics on firn stratigraphy. Our results demonstrate that the combination of multi-year GPR profiles, CMP analyses, and firn-core observations can be used to quantify temporal changes in firn density, stratigraphy, and compaction rate, an essential step toward improving firn-densification models and glacier mass-balance estimates.



1 Introduction

Firn is essentially snow that has survived at least one summer or melt season without densifying into glacier ice, which can be found in ice caps, ice sheets, and glacier accumulation areas (Cogley et al., 2011). Most firn studies on mountain glaciers focus on understanding firn properties and processes, predominantly density evolution, which determines surface meltwater hydrology and also plays a role in accurately estimating glacier mass balance from geodetically measured volume changes (Huss, 2013; Stevens et al., 2024). Further detailed study of the firn processes helps interpret the ice-core data, which provide distinct regional climate records of the high-Alpine glaciers (e.g. Arnaud et al. 2000; Fisher et al. 2006; Miller et al. 2021). There is clear evidence that a changing climate is warming the firn columns and altering the snow and firn structure and chemical composition, thereby compromising climate records (Bezeau et al., 2013; Samimi and Marshall, 2017; Ochwat et al., 2021; Horlings et al., 2022). Similarly, Williamson et al. (2020b) and Huber et al. (2024) suggest that increased snow accumulation and melt at high Alpine glaciers (St. Elias Range) increase the chances of a firn aquifer by insulating the underlying firn.

The basic understanding of firn processes, particularly influencing firn density, is well established under cold polar conditions (e.g., Herron and Langway 1980; Arthern and Wingham 1998; Li and Zwally 2004; Reeh 2008; Ligtenberg et al. 2011). However, there are few studies of firn densification in Alpine glaciers, where densification rates are higher than in cold polar regions (Kawashima and Yamada, 1997; Cuffey and Paterson, 2010). Processes such as refreezing increase the presence of meltwater in pore spaces, whereas winter conditions in high Alpine glaciers cool uppermost firn layers, influencing firn densification (Hooke et al., 1983; Schneider and Jansson, 2004). The emphasis on Alpine firn, particularly on understanding firn stratigraphy, densification, and the processes that determine firn structures, is important, and efforts are made through direct observations, geophysical methods, and modelling approaches (Ambach and Eisner, 1966; Schotterer et al., 1977; Alean et al., 1983; Blatter and Hutter, 1991; Fountain and Walder, 1998; Lüthi and Funk, 2000; Huss, 2013; Sold et al., 2015).

Long-term repeat measurements of firn properties are limited in Alpine conditions. However, studies such as Stevens et al. (2024) present the evolution of firn density derived from repeat firn core measurements at Wolverine Glacier, Alaska, and demonstrate the role of firn properties and processes in glacier mass-balance estimates. Similarly, Kindstedt et al. (2025) documents ongoing firn warming at the Eclipse Icefield, Yukon, using firn core, borehole temperature, and GPR transects along with firn modelling, but without repeat measurements. Additionally, Patil et al. (2025b) used a combination of geophysical methods, glaciological observations, and a firn densification model to investigate the firn structure and density distribution in the accumulation area of the Grosser Aletschgletscher. Meanwhile, Suter et al. (2001) illustrates the spatial distribution of cold firn and the influence of climatic variables and topography on firn distribution in the European Alps using firn cores and modelling. All of these studies resolve the vertical firn density-depth relation or firn densification, but not the firn compaction rate. To distinguish between the two, firn densification is a general increase in firn bulk density driven by multiple processes. Whereas firn compaction generally refers to the change of thickness of a certain section of the firn column due to compression by the overburden stress (MacFerrin et al., 2022).

The emphasis on firn compaction rate measurements, which are predominantly observed in polar regions, is due to the need to evaluate the ice sheet mass balance estimated from geodetically derived volume-to-mass changes, which requires a detailed



55 understanding of firn porosity (e.g., Zwally et al. 2011; Shepherd et al. 2012; McMillan et al. 2016; Smith et al. 2020). The ability of firn to retain surface meltwater depends on (i) thermal properties of firn, such as firn's cold content, defined as the energy required to warm the firn pack to the melting point (Haeberli and Alean, 1985; Suter et al., 2001; Vandecrux et al., 2019), and (ii) meltwater retention depth within the firn, which is lower in case of low-permeability near-surface ice slabs (Fountain and Walder, 1998; Vandecrux et al., 2020).

60 Conventional dry firn compaction can be divided into three stages. The first stage is defined as critical density, assumed to be dominated by processes such as grain-boundary sliding, sintering mechanism, and packing ($\rho = 550 \text{ kg m}^{-3}$). Further, power-law creep, lattice diffusion, and plastic deformation are believed to drive the second and third stages of firn compaction (Herron and Langway, 1980; Morris and Wingham, 2014). The third stage of firn compaction is very slow relative to the rate of climate change and is controlled by a reduction in the enclosed air volume, leading to pore closure ($\rho > 830 \text{ kg m}^{-3}$). The bound-

65 ary between the first and second stages of firn compaction is not well defined (Benson, 1962; Simonsen et al., 2013). The firn compaction rate in dry firn is typically governed by overburden pressure, firn temperature, and firn density (Bader, 1962; Shapiro et al., 1997). In the case of warm regions, refreezing of surface meltwater or rain within the firn pores densifies the firn (e.g., Braithwaite et al. 1994; Reeh 2008). The literature indicates that no single widely accepted model can simulate the firn compaction rate. However, there are a few in situ measurements of firn compaction rate in polar conditions.

70 The coffee-can method, as termed by Hamilton et al. (1998), is used to manually measure firn compaction by placing poles at the bottom of firn boreholes and measuring surface elevation relative to the poles. Later, the same method was automated by connecting a draw-wire sensor to the temporally continuous data-logging system in Antarctica (Arthern et al., 2010). Similarly, MacFerrin et al. (2022) deployed the same approach in 48 boreholes across eight sites in Greenland. Other methods, such as those of Morris and Wingham (2014), measured firn compaction rate using a neutron probe in boreholes by repeatedly record-

75 ing high-resolution density logs, which were used to determine the distance between adjacent layers and the logs to estimate the firn compaction rate. Whereas Hawley and Waddington (2011) applied borehole optical stratigraphy at the Greenland Summit, and the same technique was used by Hubbard et al. (2020) along with a high-resolution camera to derive measurements at millimetre-scale resolution at Derwael Ice Rise, Antarctica. All these methods aid in determining the firn compaction rate with high resolution, but are limited by the invasive in situ measurement approach.

80 In contrast, Medley et al. (2015) demonstrated a non-invasive technique for estimating the firn compaction rate using repeated airborne radar surveys by determining the radar wave speed through the firn using firn cores (invasive approach). However, this method is limited by vertical resolution, which depends on radar frequency, bandwidth, and the frequency of radar flight campaigns, but offers the advantage of more extensive spatial coverage. Similarly, Kruetzmann et al. (2011) demonstrates snow accumulation and compaction using GPR data near Ross Island, Antarctica, based on density-dependent dielectric properties

85 of dry firn from snow pits and firn cores, but does not account for differences in radar-wave velocity between reflectors. Another radar-based technique used by Case and Kingslake (2022) is the Autonomous phase-sensitive radar (ApRES), which derives the firn compaction rate by tracking the firn internal reflectors over time. Other applications of ApRES related to firn compaction and vertical strain rate in grounded ice sheets in Antarctica include Gillet-Chaulet et al. (2011); Kingslake et al. (2014); Nicholls et al. (2015).



- 90 To our knowledge, no studies have focused on Alpine firn processes and structures, or on quantifying firn densification rates using multi-year in situ geophysical and glaciological measurements. Consequently, we present the first analysis to quantify the firn compaction rate and temporal changes in firn pack, such as firn density and stratigraphy, at the accumulation area of the Grosser Aletschgletscher in the Swiss Alps. It is based on non-invasive GPR-derived geophysical measurements, primarily the common-midpoint (CMP) method, supported by direct glaciological observations, including shallow and deep firn cores.
- 95 Specifically, our study focuses on the following research questions:
- (i) What do the CMP measurements reveal about temporal changes in the firn pack?
 - (ii) Can we quantify the firn compaction or densification rate from the multi-year CMP gather?
 - (iii) How do GPR and firn core measurements reflect the effect of a warming climate and extreme Alpine summers on firn stratigraphy?
- 100 In this study, we use the dataset established in our prior work (Patil et al., 2025a), complemented by new investigations to address the limitations identified there and to extend the field observations required to quantify temporal changes in firn pack, such as firn density and compaction rate.

2 Study area

- The Grosser Aletschgletscher is the largest glacier in the European Alps (Switzerland, 46.5 °N, 8.0 °E, Fig. 1), characterised
- 105 by three large accumulation basins that converge at the Konkordiaplatz and form a 13 km long, curved glacier tongue to the south (Grab et al., 2021). The glacier area was approximately 78.5 km² in 2017, and the glacier was approximately 20 km long (GLAMOS, 2018b; Linsbauer et al., 2021). The glacier elevation ranges from 1700 to 4200 m a.s.l., while the average equilibrium line altitude (ELA) over the last decade was approximately 3160 m a.s.l. and 3185 m a.s.l. at the end of summer 2025 (GLAMOS, 2025). The glacier receives high precipitation (winter mass balance) at the accumulation area (Jungfraufirn,
- 110 Ewigschneefeld, and Mönchsloch), primarily driven by northern precipitation (Schwarb et al., 2001; MeteoSchweiz, 2025; Rückamp et al., 2025). At the central accumulation basin (Jungfraufirn), point-based surface mass balances have been measured since 1920, providing long-term annual and seasonal mass balance (Huss et al., 2009; GLAMOS, 2022). The meteorological data recorded at the weather station at 3571 m a.s.l. shows an annual mean temperature of -6.35 °C over the last 25 years (2000-2025), and a mean winter temperature (September - May) during the same period of -8.61 °C (MeteoSchweiz, 2025).
- 115 There are no precipitation observations at this site due to extreme weather conditions (e.g., strong winds).

3 Data acquisition

- Temporal changes in firn density and compaction can be investigated through multi-year or repeat measurements at similar locations. In this study, we acquired two ground-penetrating radar (GPR)-based common-midpoint (CMP) measurements and a shallow firn core in the March 2025 campaign at similar locations to those of our previous work (Fig.1 in Patil et al. 2025b)
- 120 and an additional CMP at the lower part of the Ewigschneefeld (Fig. 1). We retrieved two firn cores to compare with GPR

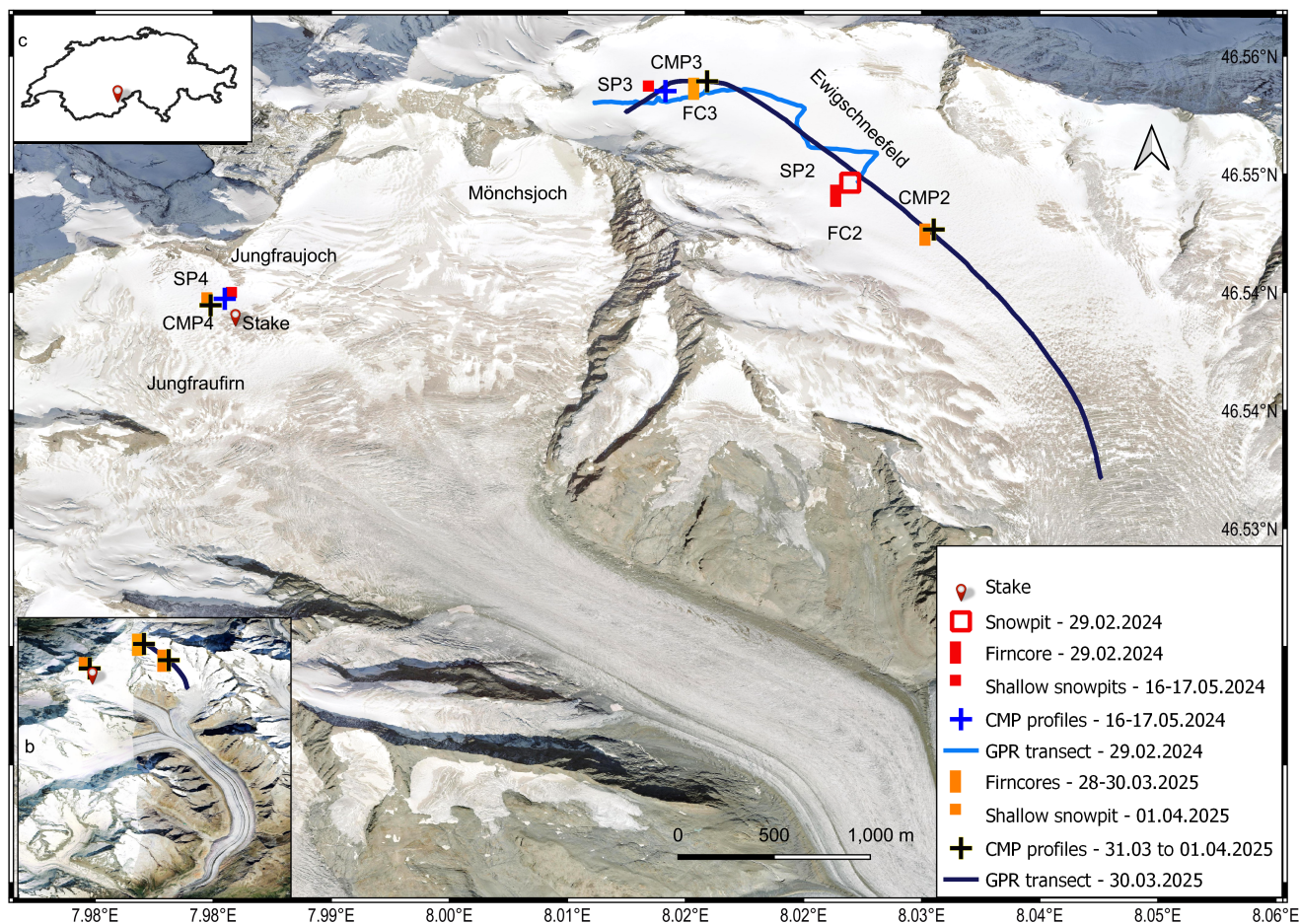


Figure 1. The Study area illustrating the upper part of the Grosser Aletschgletscher, consisting of Jungfrau firn, Ewigschneefeld, and Mönchsloch. The figure also shows the corresponding glaciological and geophysical measurements from the 2025 campaign, along with similar measurements from the 2024 campaign used in this study, as detailed in the legend. The background map shown in the figure was obtained from the Swiss Federal Office of Topography, a cloud-optimised Geo-TIFF of 2 m resolution. The inset map (b) is a satellite image of the Grosser Aletschgletscher (imagery and map data © 2024 Google). The geographical location of the Grosser Aletschgletscher is shown in the inset map (c) on the top left.



Table 1. Summary of all glaciological and geophysical measurements along with the deep firn core (FC3, in Fig. 1) acquired during the Grosser Aletschgletscher winter-2025 expedition.

Observation type	Survey date	Latitude	longitude	Elevation (m a.s.l)
Firn core (FC3, depth: 19.4 m)	28 March 2025	46.55808	8.01725	3450
Firn core (FC2, depth: 7.8 m)	30 March 2025	46.54806	8.03264	3360
CMP2	30 March 2025	46.54816	8.03277	3360
GPR transect (length: 4400 m)	30 March 2025	46.55625 - 46.53185	8.01214 - 8.04435	3514-3202
CMP3	31 March 2025	46.55829	8.01748	3450
CMP4	01 April 2025	46.54314	7.98389	3340
Snow pit (SP4, depth: 2.8 m)	01 April 2025	46.54327	7.98393	3340

measurements at the upper and lower parts of the Ewigschneefeld, respectively, and a snow pit near the mass balance stake at Jungfraufirn (Fig.1). Additionally, we collected a GPR transect on Ewigschneefeld that connects the CMP sites. All these measurements were gathered between 28 March and 1 April 2025 and are summarised in Table 1. To investigate temporal firn evolution, this dataset is complemented by field data from a previous study (Patil et al., 2025a).

125 3.1 Firn cores, snow-pit, and isotope data

We acquired an approximately 18.3 m deep firn core from the base of the 1.12 m shallow snow-pit, using an electromechanical drill (FELICS small, icedrill.ch AG. 2010; Ginot et al. 2002). The corer retrieves 0.9 m core segments (58/73 mm core/borehole diameter) at the upper part of Ewigschneefeld near the CMP3 location (FC3 in Fig. 1). This enables direct observation of the firn density profile to a depth of nearly 19.4 m. Density within the snow pit was measured using a 14 cm-long cylindrical cone with a 4.75 cm diameter. At the same time, the firn core sections were split into approximately 20 cm intervals for density determination. The initial 20 cm of the first firn core was soft, and we assumed some disturbance due to drilling during density estimation at a shallow depth of around 2-3 m. We used plastic bags and analogue weighing springs to measure the density. The 20 cm firn core sections were stored in plastic bags, melted at the research station, and the meltwater was transferred into sampling tubes. The collected samples were analysed in the laboratory of the Geozentrum Nordbayern at Friedrich-Alexander-Universität Erlangen-Nürnberg for stable isotopes (expressed as per-mil deviation from a defined standard: VSMOW Vienna Standard Mean Ocean Water) and chemical impurities (major ions).

An additional firn core of approximately 7 m depth from the bottom of a 1.12 m snow-pit was gathered on 30 March 2025, using a “Mark II Ice Coring System” from Kovacs Ice Drilling Equipment with a 9 cm diameter at the lower part of the Ewigschneefeld near the CMP2 location (orange FC2 in Fig. 1). In this case, while translating from snow-pit to firn core drilling, we expect a loss of around 15-20 cm in core length due to the crumbling of fresh snow, and the data gap is filled with an assumption of fresh snow density measured from the snow-pit. A snow pit (orange SP4 in Fig. 1) approximately 2.8 m deep was dug near the CMP4 location to measure near-surface density and to investigate melt-induced ice lenses at the Jungfraufirn. Density was estimated using the same 14 cm-long, 4.75 cm-diameter cone.



3.2 Ground-penetrating radar data

145 To investigate the spatial and temporal variations in firn density, we complemented our 2024 measurements with two CMP
measurements at similar locations (Fig.1) and an additional CMP at the lower part of the Ewigschneefeld (CMP2 in Fig. 1).
We also extended the GPR transect to trace the firn to ice transition and the variation in firn thickness with elevation along
a flow line. All three CMP measurements were collected using a 200 and 600-MHz dual-frequency, mono-static IDS GPR
system. The CMP acquisition setup used 20 cm offsets from the fixed mid-point (i.e., a 10 cm shift of the antennas on either
150 side of the midpoint), covering a total CMP measurement length of 20 m.

The GPR profile (same instrument as for the CMP) with a length of 4.4 km extends below the equilibrium line altitude (ELA),
covering an elevation range from 3514 to 3202 m a.s.l (Table 1, black GPR transect in Fig. 1) and extends beyond the 1.8 km
long GPR track from 2024 (blue GPR transect in Fig. 1). The overview of measurement locations from both winter campaigns
(2024 and 2025) is shown in Figure. 1.

155 4 Methods

4.1 GPR data processing

The GPR transect was processed using ReflexW software (Sandmeier, 2010) following the conventional processing steps
as described in previous studies (Ulriksen, 1982; Annan, 1993; Fisher et al., 1996). A sequence of processing steps, such
as filtering and gain, removes noise and improves the visibility of the radargrams. The application of the de-wow filtering,
160 stacking, and bandpass Butterworth filter increased the signal-to-noise ratio. Other processing steps, such as moving the start
time, background removal, and correction for equidistant traces, were also applied (Fig. 2a). The visible IRHs on the radargrams
were picked using the built-in semi-automated phase follower tool (Figs. 3b and c).

4.2 GPR CMP semblance analysis

Studies such as Looyenga (1965); Topp et al. (1980); Endres et al. (2009) illustrate that the subsurface properties of the medium
165 can be derived from the radar wave propagation velocity, which is necessary to accurately estimate internal reflection horizon
(IRH) depths from the measured two-way travel time (TWT). The common midpoint method (CMP) is a geophysical technique
that assumes that subsurface reflectors (IRHs in radargrams) are horizontal, homogeneous layers. The CMP acquisition is
carried out by maintaining equidistant intervals between the chosen fixed midpoint and both the transmitter (Tx) and the
receiver (Rx). With this approach, subsurface targets appear as diffraction hyperbolas in the radargram (Fig. 2a). The radar
170 propagation velocity in the medium above the target can be estimated by matching the reflections of a synthetic propagation
model to the curvature of the observed reflections (Yilmaz, 2001; Annan, 2005; Schmelzbach et al., 2012). The CMP data
processing is similar to our approach in 2024 (Patil et al., 2025b) and, as explained in section 4.1, differs only in that each
Tx-Rx offset was measured separately and subsequently combined into a continuous profile in ReflexW.

The semblance analysis (Fig. 2) aids in picking V_{rms} and TWT based on the peak energy coherence between waveforms that are

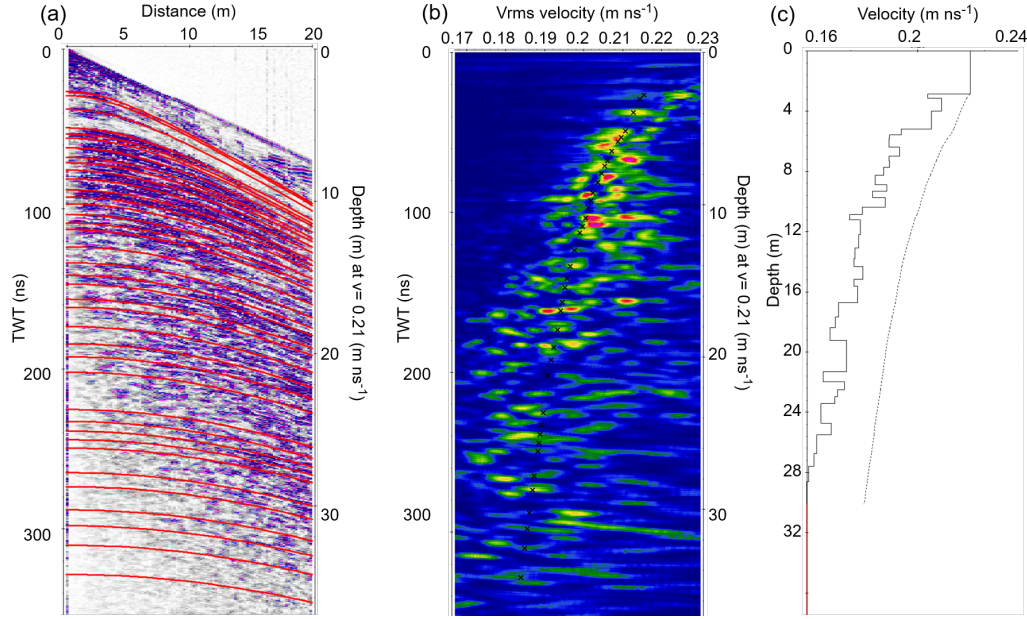


Figure 2. The semblance analysis of the common mid-point (CMP) data gathered at the Ewigschneefeld (CMP2 in Fig. 1). The picked hyperbolic pattern or internal reflection horizons (IRHs) using ReflexW software (a) matches the energy coherence (b) representing V_{rms} velocities corresponding to the semblance pick. The 1-D modelled interval velocity for the picked V_{rms} is shown on the right part (c) of the figure. The dotted line shows the picked V_{rms} , and the solid line indicates the corresponding interval velocity. The left y-axis in the figure (a and b) represents the radar wave two-way travel time (TWT) in ns. The right y-axis of the figure (a) and (b) indicates an approximate depth (m), assuming a constant radar velocity in firm of 0.21 m s^{-1} . In panel (c), the left y-axis shows the depth adjusted to the modelled interval velocity. The x-axis in panel (a) is the distance in metres, and in panels (b) and (c), the pickable V_{rms} velocity for the corresponding semblance energy.

175 centred on hyperbolic trajectories (Fig. 2b) within the analysis windows (Sheriff and Geldart, 1999). The picked V_{rms} velocities and corresponding TWT of each reflector from the semblance analysis can be used to determine the interval velocities (Fig. 2c), which is a measure of subsurface dielectric properties within each IRH:

$$V_{int} = \sqrt{\frac{v_{rms_i}^2 \text{twt}_i - v_{rms_{i-1}}^2 \text{twt}_{i-1}}{\text{twt}_i - \text{twt}_{i-1}}} \quad (1)$$

180 Where V_{int} is the interval velocity through layer i , twt_i , twt_{i-1} , v_{rms_i} and $v_{rms_{i-1}}$ are two-way travel times and root-mean square (v_{rms}) velocities through layer i th, and $i - 1$ th interfaces, respectively. Further, the density within each reflector can be obtained by using the relation between the interval velocity (V_{int}) and the density by modifying the critical refractivity index



method CRIM (Wharton et al., 1980; Knight et al., 2004) as

$$\rho = \frac{\left(\frac{V_{\text{air}}}{V_{\text{firn}}} - 1\right)}{\left(\frac{V_{\text{air}}}{V_{\text{ice}}} - 1\right)} \rho_{\text{ice}} \quad (2)$$

185 Here, V_{air} and V_{ice} are radar wave velocities in air and ice (0.3 and 0.167 m s^{-1} , respectively), whereas the velocity of the radar wave propagation within the firn layer (V_{firn}) is estimated from the Dix equation (Eq. 1) using picked V_{rms} from CMP semblance analysis and density of ice is assumed as 920 kg m^{-3} .

4.3 Internal reflection horizons as annual firn layers

Sold et al. (2015) illustrates the identification of internal reflection horizons (IRHs) as annual layers through direct compar-
190 ison with firn core observations. Patil et al. (2025b) presents an iterative chronological method to identify internal reflection horizons (IRHs) as annual layers by estimating snow water equivalent (SWE) from GPR-derived CMP-based radar velocity and comparing it with point mass-balance observations. We used this approach to identify internal reflectors as annual layers from the CMP (CMP2 and CMP4) acquisition. This is achieved firstly by determining each reflector's depth from the measured TWT, and estimating the snow water equivalent (SWE) of the respective layer by multiplying the radar interval velocity (Eq.
195 1) with the estimated density within each layer (Eq. 2):

$$\text{SWE}_{12} = 0.5 \times \text{TWT}_{12} \times V_{12} \times \rho_{12} \quad (3)$$

with $0.5 \times \text{TWT}_{12} \times V_{12}$ being the thickness of the respective layer.

The estimated SWE within each reflector was compared chronologically with the long-term point mass balance observations (Stake in Fig. 1). The matched SWE between the CMP-derived and long-term point mass balance measurements from the
200 identified IRH is treated as an annual layer; otherwise, the next reflector (IRH) is evaluated until a match is found for that particular year. This process was applied to CMP-derived reflectors at two locations (CMP2 and CMP3, in Fig. 1), assuming constant relative accumulation, which is likely to be constant over a limited area and conservation of mass within each identified annual layer.

4.3.1 Annual layer dating using firn core

205 We used spikes in chemical impurities, particularly Fe, as a summer horizon complemented by visible Sahara dust events from the firn core (FC3 in Fig. 1) to date the annual firn layers. Further, IRHs from nearby CMP3 measurement (CMP3 in Fig. 1) were identified as annual layers by chronologically comparing the estimated SWE above each Fe spike with the CMP-derived SWE (Eq. 3). The comparison of estimated SWE from point mass balance measurements (stake in Fig. 1) and FC3 is shown in the Appendix Figure A5, which is used to identify annual layers using CMP gathered at CMP4 and CMP3 locations,
210 respectively. The uncertainty associated with IRHs derived from the semblance analysis and annual layer dating is discussed in section 6.5.



4.4 Spatial firn density variation and accumulation distribution

We used a direct comparison between CMP3 and the deep firn core (FC3) at the same location, and the implications of having CMP and firn core at the same location are provided in the discussion. We estimated spatial firn density variation and accumulation distribution, following a similar method as presented in our previous work by using a CMP-derived density-depth profile (CMP2) at lower part and a firn core (FC3) at the upper part of the Ewigschneefeld, identified annual layers (sections 4.3 and 4.3.1), and estimated corresponding density within firn layers (Eq. 2). Further, we obtained the spatial firn density distribution by interpolating the density gradient along the GPR profile (black line in Fig. 1) between FC3 and CMP2 locations. The accumulation distribution can be estimated in terms of SWE by multiplying the firn layer thickness by the estimated density of the respective layer (Eq. 3). The IRHs identified on the radargram (Fig. 3b) are considered as annual layers by following the procedure in subsection 4.3. We compared the results of accumulation and density variations with those from 2024 investigations and interpreted the temporal changes. We provide corresponding figures with brief interpretation in the Appendix (Figs A3 and A4). However, we discussed their effect on temporal changes in density and compaction rate estimations within the respective discussion sections (sections 6.3 and 6.4).

4.5 Firn compaction rate

To derive the firn compaction rate from the CMP data, we compute the change in annual-layer thickness between two time points (Hawley et al., 2004), specifically between the 2024 and 2025 measurements. After identifying annual layers, we determine the change in TWT in nanoseconds (ns) and, subsequently, the depth for each layer from the interval velocity. This change in layer thickness with time provides the compaction rate.

$$\text{Compaction rate} = \frac{\text{Layer thickness}_{i,2025} - \text{Layer thickness}_{i,2024}}{\text{time}} \quad (4)$$

The equation used here (Eq. 4) results in negative values for thinning layers.

5 Results

5.1 Glaciological observations

Figure 4 demonstrates the snow and firn density-depth profiles at three locations of the Grosser Aletschgletscher accumulation area using direct glaciological observations from winter 2025 (orange coloured FC2, FC3, and SP4 in Fig. 1). The 19.4 m deep firn core shows a fluctuating firn density ranging from surface snow density of 200 kg m^{-3} to $\sim 830 \text{ kg m}^{-3}$ at around 15 m depth. The typical firn density of 550 kg m^{-3} is reached at around 5 m, and the depth of near pore close-off density (830 kg m^{-3}) is deeper than the drilling depth despite some local maxima at around 13 and 18 m, which can be attributed to increased local density due to ice lenses. The shallow firn core obtained at the lower part of the Ewigschneefeld (FC2 in Fig. 4) demonstrates a similar density-depth variation compared to that of the deep firn core (FC3), but with generally higher densities.

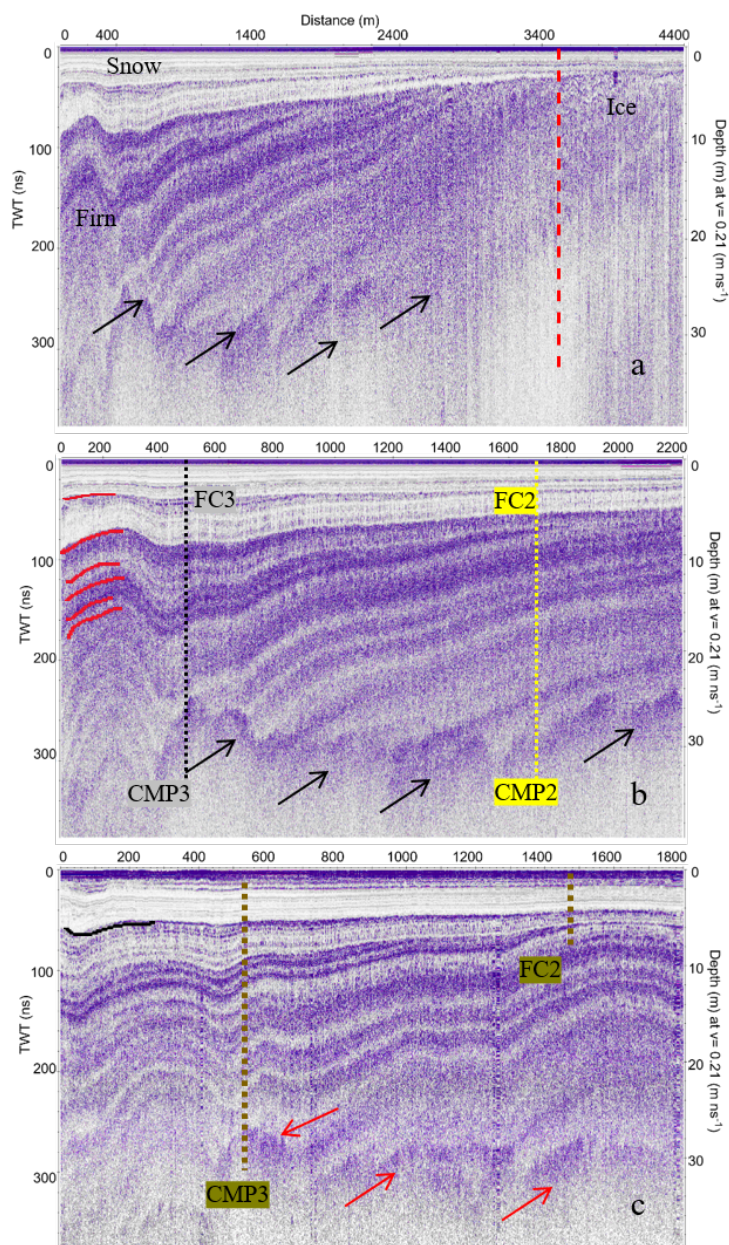


Figure 3. Radargrams obtained from the ground-penetrating radar (GPR) profiles gathered in 2025 (a), a shortened 2025 radargram (b) that covers a similar section as the 2024 radargram (c). The location of the GPR profiles is described in the data chapter (section 3). The top x-axis shows the distance of GPR profiles, the left y-axis depicts radar two-way travel time (TWT) in ns, and the right y-axis indicates the approximated depth in meters, assuming constant radar velocity in firn (0.21 m s^{-1}). The approximate locations of CMP and firn core measurements along the respective GPR profiles, as detailed in Figure 1, are indicated in the respective radargrams (b and c). The dotted vertical red line depicts the approximate location of the equilibrium line altitude (ELA). The pickable IRHs in both radargrams are shown in red lines (b) and a black line (c), and the strong reflector at the deeper depth of the radargrams is shown in black (a and b) and red (c) arrows.

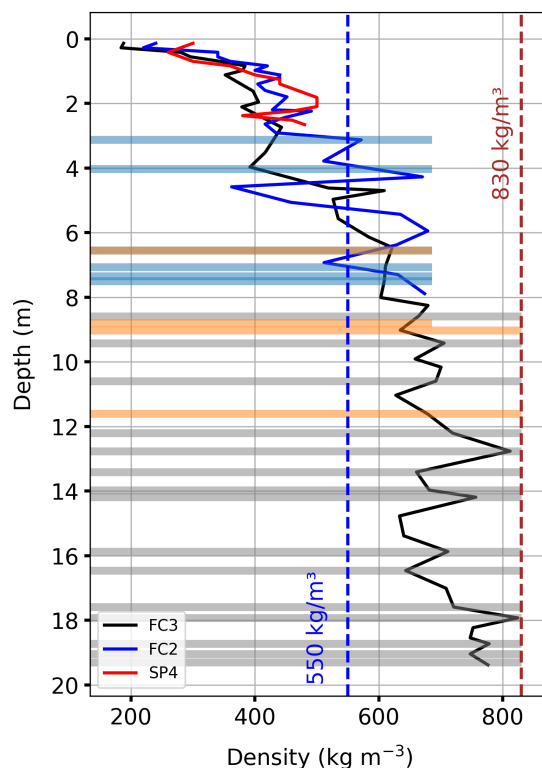


Figure 4. The density-depth profile obtained from the deep firn core (FC3), a shallow firn core (FC2), and a snow-pit (red line, SP4) from winter 2025 (Fig. 1). The light blue and grey horizontal bars represent visually identified ice lenses in the shallow firn core (blue line) and in the deep firn core (black line), respectively. Visible Sahara dust layers are shown as orange horizontal bars and a brown bar. The vertical dotted blue and brown lines indicate the firm and pore close-off density, respectively. All ice lenses and the visible Sahara dust layer thickness are not to the scale.

The depth to reach firn density (550 kg m^{-3}) is at 3-3.25 m. The density offset between FC2 and FC3 locations is pronounced at depths greater than 2 m. The estimated bulk SWE up to the common depth of around 8 m at FC3 location is around 3950 mm w.e in comparison with 4140 mm w.e at FC2.

245 Ice lenses were found in the shallow firn core (FC2) at smaller depths (around 3 m) and at the bottom of the firn core (7-7.5 m), depicting the corresponding density maxima at these depths. Whereas, within the deep firn core (FC3), we could not identify any near-surface ice lenses up to a depth of 8.5 m. Several ice lenses were identified at greater depths, corresponding to local density maxima. The visible Sahara dust layers (orange bars) can also be seen near 9 m and 11.5 m in the deep firn core (FC3) and at 6.5 m (brown bar) in the shallow firn core (FC2). The density trend from the snow-pit (SP4) shows similar variations as
 250 that of FC2, except for the higher surface snow density and a sharp kink at 2.5 m depth with a surface density offset of around 80 kg m^{-3} when compared with the FC3 measurement results.



5.1.1 Firn core-derived profiles of stable water isotope and chemical impurities

Figure 5 shows the comparison of the density (a), stable water isotope (b), and electrical conductivity (c) profiles. Whereas major ions and chemical impurities (d, e, f, and g) profiles indicate the deposition of dust and anthropogenic pollutants with depth. The variations in the $\delta^{18}\text{O}$ show pronounced signal fluctuations from the surface to a depth of 3.5-4 m. The result shows that the stable water isotope signal attenuates from 3.5 m to 9 m, and we estimate that the last summer horizon or the firn layer starts at 3-4 m depth (at the time of sampling, Table 1). The results show lower $\delta^{18}\text{O}$ concentrations of -12 to -17‰ between 4 and 8 m, which further decreases to below -12‰ between 9 and 15 m. At deeper depths (depth > 15 m), $\delta^{18}\text{O}$ concentration fluctuates between -17 and -10‰ . The electrical conductivity, which indicates total ion content in Figure 5c, shows a strong spike near 4 m depth. However, below 4 m, the electrical conductivity signal is significantly reduced, indicating loss of signal due to meltwater percolation (washout and eventual run-off of soluble ions) and a mean concentration of $5.8 \mu\text{S/cm}$. Whereas some noticeable spikes at around 9 and 13 m depth near the visible Sahara dust, and ice lenses, depict the presence of low-concentration impurities (near $15 \mu\text{S/cm}$).

Figures 5 d, e, f, and g show fluctuations in major ion and chemical impurity concentrations with depth. Of the measured species, Na is mostly associated with sea salt, with additional contributions from mineral dust, which decreases with depth, except for the spike near the identified Sahara dust and ice lenses in the firn core. While Ca, Ti, and Fe are most indicative of mineral dust (particularly Ti and Fe can also have anthropogenic sources). We identified two prominent visible Sahara dust (orange bars) events within the last 10 years from the firn core. However, three spikes in Ti mineral concentration ($>2.5 \text{ mg l}^{-1}$) at depths corresponding to two visible Sahara dust layers and one at 18-19 m depth demonstrated a possible third Sahara dust event in 2016, which we did not identify visually from the firn core. This is further evident from an increased Fe mineral concentration ($> 25 \text{ mg l}^{-1}$) at the same depth (18-19 m). The Ca ion concentration is well below 0.5 mg l^{-1} except at 3 m depth. We estimated the mean concentration of Na, Ca, Ti, and Fe as 0.34, 0.19, 0.6, and 4.8 mg l^{-1} , respectively.

Figure 5 also shows the bulk accumulation estimated from the deep firn core in mm w.e (right y-axis). We traced depth to annual layers and corresponding accumulation by considering Fe peaks as a reference to the last summer horizon. We identified that the visible Sahara dust events recorded in March 2022 and February 2021 agree well with the physically identified visible Sahara dust layers. The third Sahara dust event identified from mineral concentrations (Ti and Fe) in the firn core also matches the event observed in April 2016 (GLAMOS, 2018a).

5.2 Comparison of multi-year glaciological measurements

We compared glaciological measurements collected at similar locations on the lower part of Ewigschneefeld on 29 February 2024 and 30 March 2025. Figure 6 shows the firn cores, the snow pit-derived density-depth profiles, and the corresponding identified ice lenses and the visible Sahara dust layer during two field measurements approximately 400 days apart. The comparison of the 2024 and 2025 results shows that the depth to the last summer horizon at this elevation varies between the two years. In 2024, the measured winter accumulation up to the measurement day was approximately 1985 mm w.e (~ 5 m depth), whereas on 30 March 2025, the estimated accumulation was 1380 mm w.e (~ 3 m depth). Because of the lack of

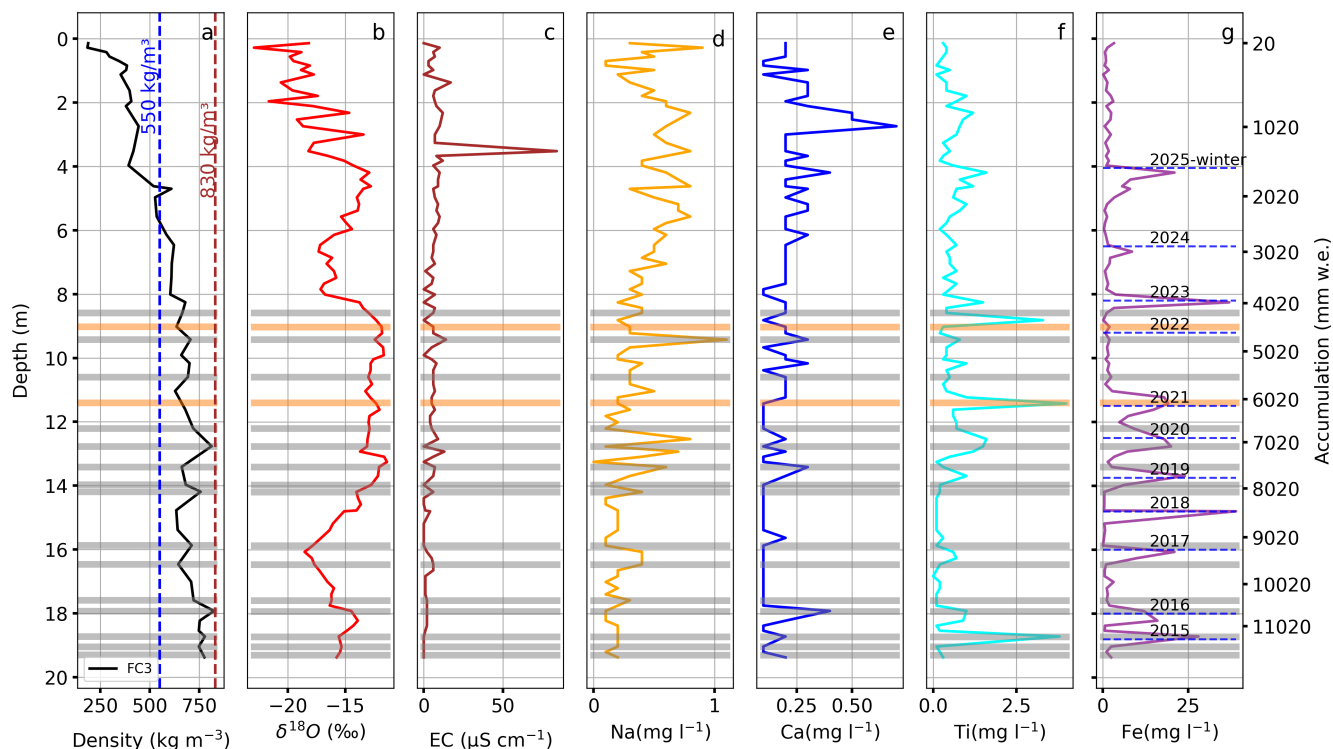


Figure 5. Illustration of depth distribution of different parameters in the firm core (a) density, (b) stable water isotope, (c) electrical conductivity, and the lab analysis of the major ions and chemical impurity concentration (mg l^{-1}) with depth, such as Na (orange, d), Ca (blue, e), Ti (cyan, f), and Fe (purple, g) for FC3 at the upper Ewigschneefeld. The firm and pore close-off densities are indicated by dotted blue and brown vertical lines, respectively (a). Grey horizontal bars represent visually identified ice lenses, whereas orange horizontal bars depict visible Sahara dust events. The highlighted dashed blue lines (g) indicate the identified annual layers. The right y-axis shows the bulk accumulation estimated from the firm core data. The thickness of all ice lenses and the visible Sahara dust layer is not to the scale.

285 isotope analysis from the shallow firm core in 2025, we can not provide further supporting evidence for the summer-to-winter transition, as compared to the firm core in winter 2024, where the result was supported by isotope analysis (see Fig. 9 in Patil et al. 2025b).

The detailed comparison reveals that the variation in density with depth remains similar up to the depth of the last summer horizon (3 m), but winter snow density at the surface in 2024 was nearly 100 kg m^{-3} less than that of 2025 measurements (depth < 1 m). The winter 2025 firm core results show significant fluctuations with a maximum density offset of 200 kg m^{-3} between 4 and 5 m depth, which is not observable in winter 2024 (FC2 and SC2-2024). This can be attributed to the observed ice lenses at that depth. Further, the depth to firm density (550 kg m^{-3}) is much shorter (depth < 4 m) in FC2-2025 compared to approximately 5 m in FC2-2024. The maximum density of around 650 kg m^{-3} occurs between 5.5 and 6.5 m in 2025, but the same can be observed at 7 m depth in the 2024 results.

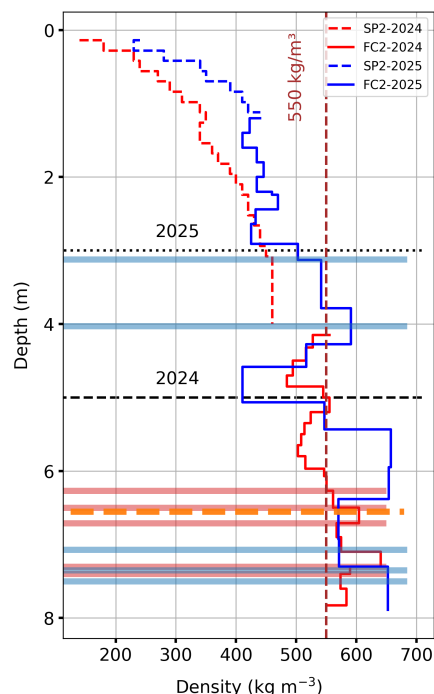


Figure 6. Comparison of firn density-depth derived from the 2024 and 2025 winter glaciological measurements (shallow firn cores, FC2 in Fig. 1) at the lower part of Ewigschneefeld. The dashed red and blue vertical lines refer to the density profiles from the snow pit, whereas the solid red and blue lines illustrate density-depth profiles derived from the firn core starting at the bottom of the respective snow pits. The horizontal lines shown here are identified ice lenses from the snow and firn cores corresponding to the coloured lines. The visible Sahara dust layer is depicted by a horizontal dashed orange line, identified from the firn core collected during the 2025 measurements. The black, dashed-and-dotted horizontal layer represents the 2025 and 2024 winter accumulations in depth meters, respectively. The legend at the top-right corner of the figure shows the years and corresponding glaciological measurements. The depth axis (y-axis) is plotted as a reference surface for the respective 2025 and 2024 shallow firn core results.

295 5.3 Radar-derived firn stratigraphy

The firn density-depth profiles of all three CMP acquisitions show the increasing density with depth. Figure 7 illustrates the variable densification across three locations of the Grosser Aletschgletscher. At the lower part of Ewigschneefeld, the identified first reflector depth is approximately 3 m, and density above the first reflector is around 450 kg m^{-3} (CMP2), which is similar to the results from the CMP4 profile with an initial density of 460 kg m^{-3} . In contrast, the CMP3 located at the higher elevation has a somewhat lower density (420 kg m^{-3}) from the surface to the first reflector depth (around 3.5 m). The depth to firn density (550 kg m^{-3}) also varies across three locations, ranging from 3-3.5 m at CMP2 and CMP4 to approximately 5 m at CMP3 (higher elevation). Similarly, the depth to pore close-off density (830 kg m^{-3}) is significantly shallower, around 18-19 m at the CMP2 and CMP4 locations, compared to 27 m at the CMP3 location.

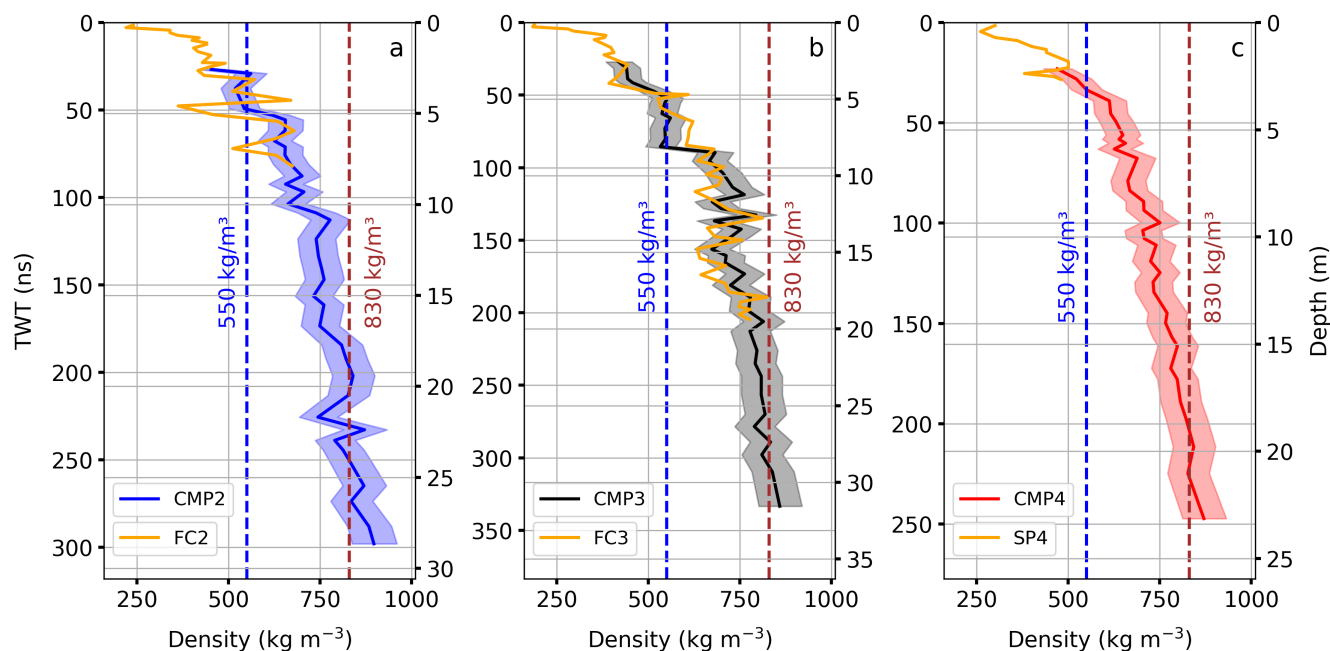


Figure 7. Firm density-depth profiles estimated from the CMP gather acquired in winter 2025 at the accumulation area of the Grosser Aletschgletscher (black crosses in Fig. 1). The figure also shows firm density-depth profiles obtained from firm cores (FC2 and FC3) and a snow pit (SP4) near each corresponding CMP measurement location (orange line in each subplot). The blue line (panel a) shows the CMP-derived (CMP2) firm density-depth profile from the lower part of the Ewigschneefeld, the black line (panel b), obtained from the upper part of the Ewigschneefeld, and the red line (panel c) shows the density-depth profile near the long-term mass balance measurement location (Jungfraufirn, Fig. 1). The uncertainty range is shown in corresponding shaded colours. The dotted blue and brown lines depict the depth to firm and pore close-off density. The left and right y-axis demonstrate the radar two-way travel time (TWT) in ns and depth in meters corrected for each of the CMP locations after the Dix equation (Eq. 2), respectively.

The comparison of the density-depth profiles between the firm core (FC3) and CMP3 measurements (Fig. 7b) illustrates similar density variations with depth. It is noticeable that certain sharp spikes in FC3 and CMP3 density measurements are located at approximately the same depths, and both show a similar depth for the snow-firm transition. The comparison of the shallow firm core (FC2) and the CMP2 density profile shows a strong spike at 5 m depth in the firm core, and a similar spike is visible in CMP2 near 4.5 m depth (Fig. 7a). The radar-derived depth to the deepest discernible IRH at all locations also varies, from 23 m (CMP4) to 27 m (CMP2) and up to 32 m (CMP3). The uncertainty of radar wave velocity determination from the semblance analysis increases with depth, as seen on all three CMP density-depth profiles in Figure 7 (shaded area).

5.4 Firm stratigraphy from GPR profiles

The radargram obtained from the 4.4 km-long GPR transect collected on 30 March 2025 is shown in Figure 3a. The depicted radargram spans ~300 m surface elevation range (Table. 1), starting at the upper accumulation area (left side of Fig. 3a) and



reaching into the ablation area of the Ewigschneefeld. Between 0 and 3500 m, the visible IRHs show decreasing thickness
315 with increasing distance along the profile. We identified the upper white region of the radargram, preceding the first prominent
IRHs, as accumulated winter snow from the 2024/2025 winter; below, IRHs are interpreted as firn layers. At the far right end
of the radargram, it is difficult to distinguish between IRHs, which can be interpreted as ice. At a depth below 25 m (~220 ns),
a prominent undulated reflector is visible (black arrows in Fig. 3a), which spans approximately between 200 and 2500 m in
distance within the accumulation area. It is evident that the total firn thickness reduces with the elevation, and almost no firn
320 exists from 3500 m onwards (~3200 m a.s.l.) (rightmost part in Fig. 3a). There, no distinct IRHs are visible except the 2025
winter accumulation and glacier ice boundary.

Figure 3b and c illustrate the comparison of the processed GPR long profile radargrams acquired on 30 March 2025 and 29
February 2024. Here, we use only the upper 2.2 km of the 2025 profile, which also covers the extent of the 2024 profile
(Fig. 3b). The first reflector between the surface and 60 ns (4.5 m) depth in Figure 3c (black line) depicts the 2024 winter
325 accumulation, which is overlaid by the 2025 winter accumulation of approximately 3 m depth (40 ns) in Figure 3b (red line),
Both radargrams show various distinct IRHs, with a prominent reflector at approximately 240 ns (24 m) in 2025 (Fig. 3b, black
arrows) and 260 ns (26 m) in 2024 (Fig. 3c, red arrows), along the GPR transect.

5.5 Radar-derived temporal change in firn density

The temporal changes in firn density at the accumulation area of the Grosser Aletschgletscher from the CMP measurements are
330 shown in Figure 8. We identified more than 30 IRHs in each CMP3 and CMP4 measurement in both years (2024 and 2025).
The use of a 600 MHz GPR system in 2025 provides higher resolution but less penetration depth than the 500 MHz GPR sys-
tem used in 2024. Therefore, we present CMP results to a common depth from all CMP measurements. It is also evident from
Figures 8a and b that the radar wave attenuates faster in the presence of denser firn (CMP4), providing the deepest discernible
IRH approximately at 23 m depth. In contrast, at the CMP3 location, the deepest IRH is at nearly 33 m.

335 The comparison of temporal changes in CMP-estimated firn density at the CMP3 location (Fig. 1) shows an increase in firn
density with depth, with some fluctuations along the profiles occurring at similar depths. It is observable that the firn density
profile from 2025 (black line in Fig. 8a) shifted towards higher values compared with the 2024 CMP measurements. The depth
to the firn density (550 kg m^{-3}) is around 7 m in 2025 and 8 m in 2024, and the pore close-off density (830 kg m^{-3}) is reached
at approximately 27 m in 2025 and 2024 measurements. Similarly, increased firn density with depth is seen in Figure 8b, esti-
340 mated from CMP4 measurements near the Stake (Fig. 1), which is located at a lower elevation than the CMP3 measurements.
Comparison of firn density-depth profiles shows a distinct, higher density shift in 2025. The depth to firn density is at around
3.5 m in 2025 and 8 m in 2024, whereas the pore close-off density is observed at approximately 19 m in both years.

Figure 9 represents the temporal changes within the identified annual firn layers using 2024 and 2025 CMP measurements at
two locations of the accumulation area of the Grosser Aletschgletscher. As explained in the method section (section 4.3), we
345 identified 10 and 11 annual layers from more than 30 IRHs at CMP3 (Fig. 9a) and CMP4 (Fig. 9b) measurements. At the CMP3
locations, firn density within the annual layers is higher than in the 2024 measurements. The 2025 winter accumulation shows
a lower snow density (430 kg m^{-3}) than the 2024 winter accumulation, which is close to 500 kg m^{-3} (orange line in Fig. 9a).

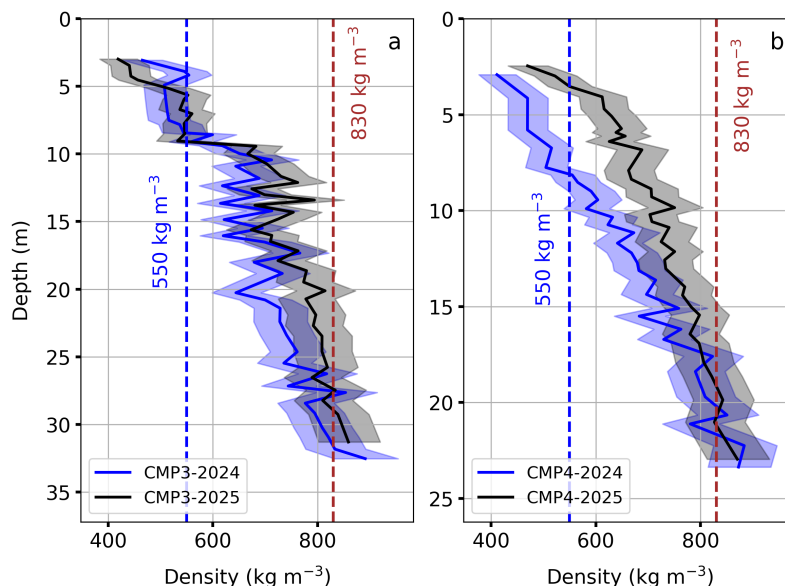


Figure 8. Comparison of the CMP-derived firn density-depth profiles obtained at the upper part of Ewigschneefeld CMP3 (a) and near the stake CMP4 (b) during the 2024 and 2025 winters. The colours refer to 2024 (blue) and 2025 (black) measurements. The blue and brown dotted vertical lines indicate the depth to reach firn and pore close-off density, respectively. The firn density-depth profiles are plotted along with the uncertainty in V_{rms} picking (0.005 m ns^{-1}) from Semblance analysis as a corresponding coloured shaded area.

We estimated an increase in density offset across all identified layers from 2024 to 2025, with the change more pronounced in layers 3 and 4 (years 2022 and 2021). The results indicate that the effect of densification is low in deeper or older layers (layers 9 and 10 correspond to 2016 and 2015, respectively), and the estimated density within the identified oldest layer (2015) is approximately 750 kg m^{-3} . The identifiable 2022 firn layer at the CMP3 location densified from 540 kg m^{-3} in 2024 to 610 kg m^{-3} in 2025.

Similarly, the CMP4 results show pronounced firn densification in the near-surface annual layers (2023 and 2021), with complete ablation of layer 3 (2022) at this location. The maximum densification is around 140 and 100 kg m^{-3} per year in the 2023 and 2021 firn layers between 2024 and 2025. The estimated density change (offset) within older layers (2017 to 2014) is small. The density difference between the winter 2024 and 2025 accumulation (orange line in Fig. 9b) is not as significant as recorded at the CMP3 location (near 40 kg m^{-3}). The identified oldest layer (2014) has a density near the pore close-off density (830 kg m^{-3}) in the 2024 and 2025 measurements. Whereas, the 2024 winter-accumulated snow densifies further, from 450 to 620 kg m^{-3} in 2025. Figure A6 also depicts a form of visualisation of the temporal changes in firn density within identified annual layers at two locations.

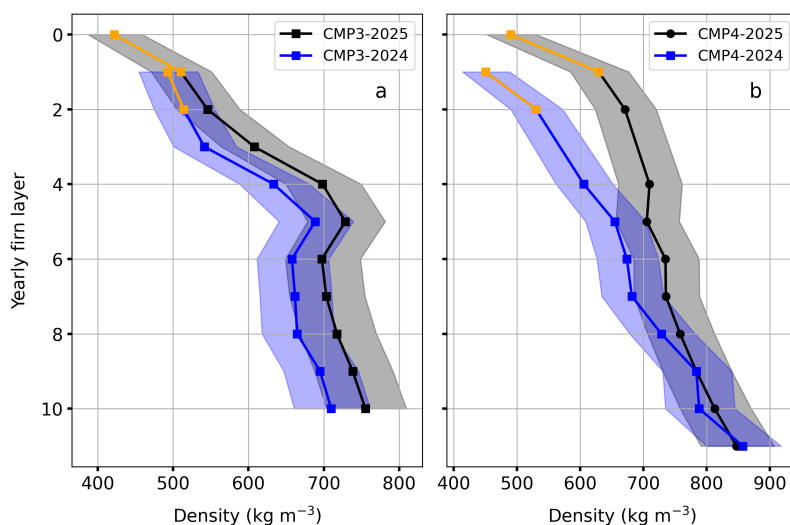


Figure 9. Illustration of the temporal density change in annual layers at the upper part of Ewigschneefeld from CMP3 measurements (a) and identified from CMP4 measurements near the stake (b). Blue lines in both plots (a and b) depict the density in 2024, whereas the black lines show the density from the 2025 winter measurements. The corresponding coloured shaded area represents the uncertainty in density estimating due to the changes in V_{rms} picking (0.005 m ns^{-1}) from the Semblance analysis. The orange line in both plots represents the winter accumulation density (from the surface to the last summer horizon) for each year. The y-axis depicts the number of firn layers in descending order, with reference to the 2025-winter surface as zero and the deepest layer 11 as 2014.

5.6 CMP-derived firn compaction rate

The CMP-derived compaction rate of commonly identified annual layers at both CMP3 and CMP4 locations is shown in Figure 10a, and the corresponding temporal change in firn density is depicted in Figure 10b. We estimated that commonly identified annual layers, particularly those near the surface (younger layers), compacted by nearly 0.3 m a^{-1} at the CMP4 location (red line). In contrast, the compaction rate of the same layers at the CMP3 location was approximately 0.2 m a^{-1} . The compaction rate of the deepest layers at the CMP3 and CMP4 locations is nearly zero. The estimated bulk compaction from the reference surface (layer 0 as 2023) to the common firn layer (layer 8 as 2015) at CMP3 is 0.5 m, and at the CMP4 location is 1.18 m between the 2024 and 2025 measurement periods. The mean compaction rate of commonly identified annual layers from 0-8 (2023 to 2015) at the CMP4 location is approximately -0.14 m a^{-1} , whereas at the CMP3 location it is approximately -0.06 m a^{-1} . It is noticeable that the higher compaction of younger layers and lower compaction of older (deeper) layers correlates well with the observed change in firn layer density over a year (Fig. 10b).

Cumulative depth-age Figures 11a and b illustrate that the depth of commonly identified annual layers from the referenced layer (2023 as layer 0) to the last identified layer 8 (2015) in both measurement years at CMP4 and CMP3 locations. At the CMP3 location, the cumulative depth of 9 identified annual layers is approximately 11.52 m in 2024, compacted to 11 m in 2025. The compaction is most pronounced in the near-surface layers (Fig. 10a), as reflected by the close spacing of layers

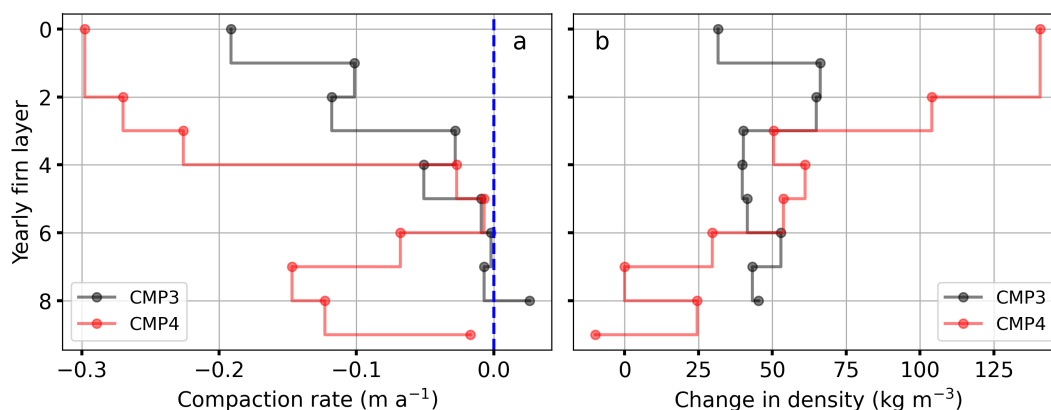


Figure 10. Illustration of the compaction rate (a) and change in density-age (b) within annual layers derived at the upper part of the Ewigschneefeld (CMP3, black line) and near the stake (red line) during the 2024 and 2025 expeditions. The vertical dotted blue line indicates zero compaction rates. The y-axis depicts the yearly firm layers with reference layer zero as year 2023 and the deepest layer 9 as year 2014.

0–3 compared to the deeper layers (4–8), which are nearly parallel. Whereas at the CMP4 location, the total thickness of the 8 identified annual layers is around 13.4 m in 2024 and 12.2 m in 2025 measurements. Similar to the CMP3 location, the effect of compaction is pronounced in near-surface layers (0-4). As mentioned previously, the affect 2022 extreme summer melt completely ablated layer 1 at the CMP4 location, which is identifiable at the CMP3 location, resulting in a thicker firm body of around 8 m up to layer 6 in 2025 compared to 6 m at the CMP4 location. The overall bulk thickness from 0-9 layers at the CMP4 location is almost similar to that of the CMP3 location, which we attribute to the uncertainty (Figs. A5 and 5) in annual layer dating using the firm core (FC3, method section 4.3.1) as discussed in section 6.5.

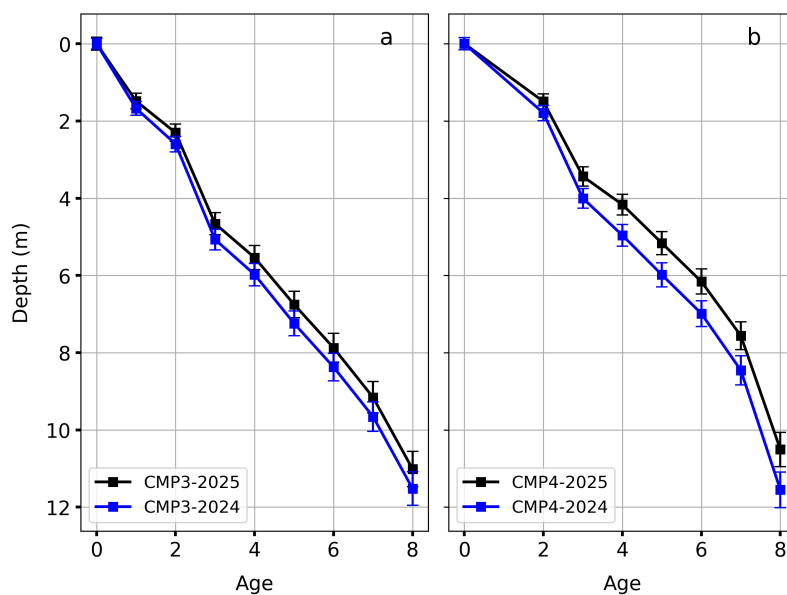


Figure 11. The depth-age plot derived from the CMP measurements at the upper part of the Ewigschneefeld CMP3 (a) and near the point mass balance measurement CMP4 (b) in 2024 and 2025. The blue line shows the cumulative depths of all identified common annual layers derived from CMP3 and CMP4 measurements in 2024. The black line depicts the CMP3 and CMP4 measurements in 2025. The x-axis depicts the number of firn layers in descending order (left to right), with reference to the 2023 annual layer as zero and the deepest layer as 2015. The error bars of the corresponding colours illustrate the V_{rms} sensitivity (0.005 m ns^{-1}) of depth estimations from the Semblance analysis.



6 Discussion

6.1 Stratigraphy from firn cores

385 The direct observations acquired at three sites of the accumulation area reveal some similar firn features as well as site-specific, distinctive firn stratigraphy. The deep (FC3) and shallow (FC2) firn cores gathered at the upper and lower parts of the Ewigschneefeld (Fig. 1) give a similar firn density-depth profile, which increases with depth. We observed a slight decrease in surface snow density at the FC3 (3450 m.a.s.l.) compared with the FC2 (3360 m.a.s.l.) locations, which we attribute to the temperature lapse rate, resulting in high-density snow. This is further evident from the SP4 (3340 m.a.s.l.) density-depth
390 profile, which shows a higher surface density of 80 kg m^{-3} (Fig. 4) than FC3, consistent with the other observation. Our results indicate that depth to the last summer horizon can be estimated from FC3 and FC2 measurements (approximately 3.5 m). This is supported by the visible ice lenses and a local increase in firn density from 420 to 550 kg m^{-3} at the FC2 location. Unlike in FC2, we did not identify any distinctive ice lenses at shallower depths (3-4 m) in FC3, which we attribute to less surface melt to form noticeable ice lenses at higher elevation ($> 3440 \text{ m a.s.l.}$). All individual results indicate a well-defined summer layer
395 beneath the winter snow in 2025 (Figs. 5b and c). We interpret the identified ice lenses as evidence of melting and refreezing events, which reflects weather patterns during their formation.

The isotope results show clear variation up to shallower depths ($< 4 \text{ m}$), indicating variations in winter precipitation. The range of $\delta^{18}\text{O}$ isotope ratio -24‰ and -12‰ lies within the expected values for the altitude (Schotterer et al., 2004), indicating preservation of both winter and summer accumulation in the upper 0-4 m. However, the signal is strongly smoothed, showing
400 little to no seasonal variability (low winter, high summer values) below 4 m depth, suggesting the effect of the 2024 summer surface melt. In addition, attenuation in $\delta^{18}\text{O}$ between 8 and 14 m depth might be attributed to the effect of extreme summer melts in 2022, which diluted isotopic signals at that depth, indicated by many ice lenses, suggesting the depth corresponding to refreezing of the melted summer snow (Fig. 5b). Schotterer et al. (2004) demonstrate that the ice core studies in the Swiss Alps and results from an ice core drilled at Jungfrauoch Saddle in 1987, exemplify the effects of wind and surface melt on
405 smoothed $\delta^{18}\text{O}$. Similarly, a sharp peak in electrical conductivity (nearly $80 \mu\text{S/cm}$ at $\sim 3.5 \text{ m}$ in Fig. 5c) provides independent validation for identifying the origin of the last summer horizon, complementing the other results (Figs. 5b and c). We attribute the smoother electric conductivity signal below 4 m to signal loss due to surface meltwater washout and the eventual run-off of soluble ions. Further, a visible rise in electrical conductivity concentrations between 8 and 15 m depth is observed, possibly driven by melt-induced impurities from the extreme summer in 2022 (Fig. 5c).

410 The analysed chemical impurities (Na, Ca, Ti, and Fe in Fig. 5) in the firn core reflect the atmospheric pollution history from anthropogenic and natural sources (e.g., Schwikowski et al. 1999; Clifford et al. 2019; Eichler et al. 2023). However, surface melt effects can significantly disturb these archived records in the ice by altering their signal preservation (e.g., Avak et al. 2018; Huber et al. 2024), as evidenced by the loss of signal strength with depth (Fig. 5). Our annual layer dating at the CMP3 location is based on spikes in Fe concentration, complemented by Ti and visible Sahara dust layers (Fig. 5g), because Ti and
415 Fe, in particular, are less affected by meltwater infiltration and are better preserved. In contrast, Na and Ca are relatively soluble and are diluted by meltwater percolation (Avak et al., 2018, 2019).



A detailed comparison of the FC2 2025 and 2024 results is shown in Figure 6, which illustrates temporal changes in the firn density features. Winter 2024 was relatively intense with a total accumulation of around 3000 mm w.e, whereas the 2025 winter accumulation is approximately 1900 mm w.e (GLAMOS, 2025), indicating changes in seasonal accumulation patterns over two winters. This is further evident in our two firn core measurements, indicating variability in fresh snow density and the depth to last summer horizons (3.25-3.5 m, 1700 mm w.e in 2025, and 5 m in 2024), which we attribute to changes in winter accumulation. The surface-melt-induced ice lenses in summer 2024 were observed in FC2 2025 measurements below 3 m depth, thereby increasing the density to near 600 kg m^{-3} at 4 m depth; the same density was observed at 6.5 m depth in 2024. We interpret that the observed identifiable cluster of ice lenses at 6.25-6.5 m depth in 2024 is still visible at 6.8-7.1 m depth in 2025 measurement (Fig. 6). This 0.3-0.75 m shift in ice lenses over a year suggests the effect of additional winter 2025 accumulation. Because our FC2-2025 measurement was on 30 March 2025 and due to the high winter accumulation in 2024, we are uncertain about the location of the 2023 annual layer. However, we roughly interpret the ice lenses at around 7 m depth to represent the 2023 annual layer (Fig. 6), considering the 3 to 4 m 2025 winter accumulation (about 2000 mm w.e), resulting in a nearly 3.5 m thick 2024 firn layer.

6.2 Radar-derived density profiles and spatial firn stratigraphy

The GPR-based CMP measurements provide an indirect firn density-depth profile, which we compared with the firn density derived from direct observations, FC3 (Fig. 1) near the CMP3 location (Fig. 7b). The profiles show similar structure, represented by a sharp rise in density at similar depths (~5, 12, 14, 16, and 17 m in Fig. 7b). These observed density spikes indicate the presence of ice lenses at the corresponding depth (Fig. 4). Both observations show a good agreement in the upper part, which corroborates the usage of CMP measurements for density estimates. Additionally, all three CMP results show the available firn thickness at the accumulation area of the Grosser Aletschgletscher, with the highest at the Ewigschneefeld (CMP3) and the lowest at the Jungfrau firn (CMP4 near the Stake in Fig. 1). Similar firn thickness was also observed in earlier studies Oeschger et al. (1977); Lang (1981), illustrating firn-ice transition depth of 32 m at the Grosser Aletschgletscher.

The radar wave penetration depth varies across the glacier (~ 32 m at CMP3, ~28 m at CMP2, and ~23 m at CMP4 in Fig. 7), which we attribute to radar wave attenuation due to increased firn density with depth, altering the dielectric property of the medium (Davis and Annan, 1989). The estimated variability in depth to firn and pore close-off density at all CMP locations illustrates spatial variation in firn densification. This is predominantly due to processes such as melt and refreezing, which increase firn densification at CMP4 compared to the other two CMP locations. We attribute the melt and refreezing processes to be elevation-dependent and minimal at the CMP3 location.

In the GPR transect data, we interpret the first pronounced reflector as the 2025 winter accumulation depth (Fig. 3a). The thickness of the snow layers is decreasing (accumulation gradient) from ~30 to ~20 ns up to 2000 m along the GPR profile, with an observable layer thinning from ~20 to 15 ns between ~2000 and 4400 m. This indicates the effect of spatial variability in winter accumulation across the GPR profile. Figure 3a illustrates that at a distance of ~3500 m onwards, the visible IRHs below the winter 2025 accumulation disappear. This can be attributed to the transition to the ablation area and to the approximate location of the ELA, which matches the ELA location reported in GLAMOS (2025). We compared the upper 2.2 km of the GPR profile



(Fig. 3b) with our 1.8 km long GPR profile gathered on 29 February 2024 (Fig. 3c). Processes such as compaction due to total winter accumulation (3000 mm w.e., thickness > 6 m) and melt and refreezing are significant at the lower part of the GPR profile (distance > 1200 m). As a result, in both radargrams, near-surface IRHs (Figs. 3b and c) and all distinguished IRHs (Fig. 3a) are thinning with the increased distance and decreasing elevation, for example, a picked IRH thickness approximately at 120-140 ns (left of Fig. 3b) is reduced to ~120-130 ns at ~1500 m distance (Fig. 3b). This supports the effect of melt-induced ablation due to lapse rate and variable accumulation.

The observed strong reflector at the deepest depth, which extends over the accumulation area (0~2400 m), was identified as an annual layer in 2024 (Fig. 3c). However, from the 2025 GPR radargram (Figs. 3a and b), we speculate that this reflector is a boundary that divides the glacier into cold and temperate zones or might have resulted from glacier dynamics. Further, the reflector is uneven, unlike the remaining IRHs, deeper IRHs (depth > 250 ns) originating from this reflector (black arrows in Figs. 3a and b), eventually reach the surface (distance > 2400 m). Similarly, at the start of the GPR profile, identifiable IRHs on the radargram are wave-like or undulated, and their smoothness increases with distance. This is also confirmed by the radargram obtained using an 800 MHz GPR system on 31 March 2021, as presented in the Figure. 5c in the Bannwart et al. (2024) study. This behaviour in firn stratigraphy is very likely due to a strong accumulation gradient near the saddle. The study by Leinss and Bernhard (2021) presents the velocity dynamics of the Grosser Aletschgletscher using TanDEM-X and GPS stake measurements, exemplifying the presence of deep firn at Ewigschneefeld, and estimates a minimal mean annual velocity of around 35-70 m yr⁻¹. Considering the lower surface velocity at this location, we hypothesise from the field observation that the ridge that separates the Ewigschneefeld from Mönchsjoch (Fig. 1) and the crevasse next to the ridge towards the Ewigschneefeld might have also contributed to the undulated firn stratigraphy (distance 0-500 m in Figs. 3b and c) along with the accumulation gradient and strong wind redistribution, however we need further research to support our interpretation.

6.3 Radar-derived temporal changes in firn density

Studies such as Sold et al. (2015) suggest that melt and refreezing can produce high-density layers, or ice lenses, that can be misinterpreted as annual layers. Therefore, not all IRHs necessarily represent annual layers, which is also clear from the comparison of density-depth profiles between firn core (FC3) and CMP3 (Fig. 7b). The method explained in section 4.3, which is introduced in Patil et al. (2025b), was used to identify IRHs as annual layers (Fig. A2a). Figures A2a demonstrate the annual layer identification by chronologically comparing CMP-derived SWE with point mass balance estimations (section 4.3), whereas Figure A2b shows the layer dating using CMP3-estimated SWE and FC3 (section 4.3.1). Thus, the identified annual layers from multi-year CMP measurements at two locations (CMP3 and CMP4 in Fig. 1) are shown in Figure 9, illustrating temporal changes in firn density within these layers. It is noticeable that the firn density has increased over the year at both CMP locations. The density-depth profiles at CMP3 show that the vertical structure of the density variations is preserved, while the absolute values increase. We attribute variations in densification at this location primarily to compaction of accumulated snow, where surface melt is generally negligible. The change in density within identified annual layers over the year increases and is highest (~70 kg m⁻³) in layers 3 and 4 (2022 and 2021) and is relatively low within older layers (~40 kg m⁻³ in 6-10 layers). Several studies have shown that the firn layers with initial lower density densify faster than the firn layers with



485 initial higher density (e.g., Gerland et al. 1999; Fujita et al. 2014). This aligns with our results from the CMP3 location, where shallower layers (3-4) densify faster than older layers (7-10) from 2024 to 2025 measurements. This suggests that processes such as pressure sintering dominate densification in denser layers with densities above 550 kg m^{-3} (Maeno and Ebinuma, 1983; van den Broeke et al., 2008).

According to Sorge's law, the density of snow does not change with time at a given depth below the surface, provided no melting occurs in summer (Bader, 1954). This is valid at the CMP3 location, as supported by our results (Fig. 8a), which demonstrate increased density with depth and show similar density fluctuations at nearly the same depths in 2024 and 2025. Further, we also observe the depth to firn density at around 7-8 m and pore close-off density at around 25-26 m in 2024 and 2025. A similar study by Stevens et al. (2024), but using direct observations (firn cores), addresses firn density evolution over a temporal scale (2016-2022) at Wolverine Glacier, Alaska, and demonstrates the importance of firn properties for glacier mass-balance estimates. Here, we show that temporal firn variations can be detected and quantified with CMP methods, which is important for characterising the climatic impact on the firn body. Although firn-core data remain necessary, CMP offers a faster approach with greater penetration depth than traditional, time- and labour-intensive firn core methods.

The changes in firn density at the CMP4 location (Fig. 1) are mainly driven by summer surface melt and refreezing in addition to compaction, because it is located at a lower elevation than CMP3 (Table 1). This is evident from the significantly higher densification rate, i.e., layer 2 densified from 520 kg m^{-3} to 680 kg m^{-3} and layer 4 from $600 - 700 \text{ kg m}^{-3}$ (Fig. 9). Studies such as Colbeck (1978); Kawashima and Yamada (1997) demonstrate firn density as a power-law dependency on time while the densification rate increases exponentially with pressure, which we also attribute to our results at this location. Further, a shift in depth to firn density over a year at the CMP4 location (Fig. 8b), which is approximately 7.5 m in 2024 and 3.5 m in 2025, indicates that the firn is densifying faster at shallower depths. This is explained by additional compaction between two measurement periods (Table 1), predominantly due to intense 2024-winter accumulation, the refreezing of surface melt in 2024-summer, and an additional accumulation layer in 2025-winter. However, this is not the case at the CMP3 location (Fig. 8a), where surface melt is likely much lower, and percolation plays a minor role, thus densification is significantly lower in layer 2 ($520-550 \text{ kg m}^{-3}$). This implies that the firn densifies faster at low-lying locations compared to firn located at higher elevations, demonstrating different climate settings at two locations of the glacier accumulation area.

We further estimated the spatial changes in firn density (Fig. A3) and accumulation (Fig. A4) by interpolating density gradient and estimating the SWE (section 4.4) between two CMP gathers at the upper and lower parts of the Ewigschneefeld (Fig. 1) using picked IRHs from the long GPR transect acquired in 2025 (Fig. 3b). Similar to the 2024 results presented in Patil et al. (2025b), our new results show that spatial firn density increases with increasing radar profile distance and decreasing elevation. This further illustrates that the same firn layers at lower elevations are denser than those at higher elevations, whereas the thickness of annual layers reflects differences in spatial accumulation variation.

6.4 Firn compaction rate and role of extreme summers

Our attempt to estimate the compaction rate in an Alpine glacier using CMP measurements will contribute new information to this poorly resolved issue. Figures 10a and 10b illustrate the estimated compaction rate and the corresponding change in



density at two locations in the Grosser Aletschgletscher accumulation area, respectively. The change in density at the CMP4
520 location is greater in the near-surface annual layers 0 and 1, which represent 2023 and 2021. This results in higher compaction
(0.3 m a^{-1}), which is hypothesised to be driven by reduced firn air content (Pfeffer and Humphrey, 1996). We speculate that
not only compaction due to overburden stress resulted from the 2025 winter accumulation, but also the summer melt (Appendix
Fig. A1) and refreezing of the 2024 accumulation, which was recorded as the highest in the last 20 years ($\sim 3000 \text{ mm w.e.}$,
in Fig. A1), have contributed to a higher compaction rate. The recorded point mass balance measurement near the CMP4
525 location indicates an annual mass balance (year 2024) at the end of the summer seasonal measurement is around 2000 mm
w.e. Additionally, the meteorological data suggest that the mean surface temperature at 3570 m a.s.l. in 2024 July and August
months was around 2.3 and 3.2°C and in 2023 was around 1.4 and 1.0°C (MeteoSchweiz, 2025), therefore, we expect a more
pronounced surface melt at 3340 m a.s.l. near the CMP4 location. Assuming partial meltwater percolated down and refroze at a
certain depth within the 2024 winter accumulated snow, and compacting it further, which increases the density from 450 to 620
530 kg m^{-3} (Fig. 9b). The process of refreezing in the 2024 summer and the accumulation of 2025 winter snow further compacted
the 2023 layer from 530 to 680 kg m^{-3} and the 2021 layer from 600 to 700 kg m^{-3} . This change in density corresponds to
compaction rates of 0.3 and 0.26 m a^{-1} in the 2023 and 2021 layers, which we interpret as reasonable estimates. Whereas
compaction in the deeper layers is primarily driven by overburden stress from the denser 2023 and 2021 firn layers, thus
yielding minimal compaction rates. This implies that the compaction rate decreases gradually with age; we estimated almost
535 zero compaction within deeper layers (layers 4-6 in Fig. 10a), which are already denser than near-surface layers and require
more time to compact further. Thus, we highlight the importance of surface meltwater percolation in resolving compaction
rates within the firn pack. The same is highlighted by (Stevens et al., 2024), suggesting the importance of considering the effect
of meltwater percolation on compaction rate to improve firn modelling in mountain glaciers.

However, at the upper part of the Ewigschneefeld, where summer melt is relatively low, we expect minimal refreezing of the
540 2024 surface melt without producing ice lenses, which is also evident from our firn core results (no ice lenses, FC3 in Fig. 4).
This is observed from the density change (30 kg m^{-3}) in the near surface annual layer 0, represents 2023 (Figs. 9a and 10b)
as well as the compaction rate of around 0.19 m a^{-1} (Fig. 10a), which we ascribe to the overburden stress from accumulated
snow. The presence of the firn layer 1 (2022 in Fig. 10) at this elevation experienced an increased change in density (nearly 70
 kg m^{-3}) with an estimated compaction rate of 0.2 m a^{-1} , predominantly due to a $\sim 9 \text{ m}$ thick accumulation on top of this layer.
545 We attribute the increase in density within layer 1 (2022) to the fact that firn density increases with pressure (Kawashima and
Yamada, 1997). Even though the change in density is decreasing in layers 2, 3, 4, and 5, whereas the compaction rate in certain
layers (3 and 4) is increasing, this is inconsistent with our results from the CMP4 location. This discrepancy likely arises from
uncertainty in picking denser but relatively thin layers (2020, 2019, and 2018 in Fig. A1). We discuss these uncertainties in the
subsequent section.

550 Figure 11 demonstrates the depth-age (depth-firn layers) from the referenced year 2023 (layer 0) to commonly identified
annual layers at CMP3 and CMP4 locations (layer 8, 2015). The observed changes in depth to annual layers in 2024 and
2025 (Fig. 11a) are closely related to the estimated compaction rates at the CMP3 location (Fig. 10a). Annual layers appear
closer to each other when compacted more (layers 0-4), and layers with minimum compaction are almost parallel to each



other. This observation also holds at the CMP4 location, where the near-surface layers (0-4) are non-parallel and exhibit a
555 higher compaction rate than the older layers (4-8). The comparison of the CMP3 and CMP4 depth-age plots shows that the
cumulative depth of 7 layers at the CMP3 location is approximately 8 m, whereas at the CMP4 location, it is 6 m in 2025. This
is mainly attributed to the ablation of the 2022 layer at this location. However, the total depth to layer 8 at both locations is
nearly the same (11 m), indicating that layers 6-8 are thicker at the CMP4 and relatively thinner at CMP3. We expect that the
identified similar layer (layer 8) should appear at a greater depth at the CMP3 location than at the CMP4 location, due to better
560 preservation of firn layers where surface melt is relatively less. The existence of the 2022 layer should also lead to a higher
cumulative thickness for all identified layers at the CMP3 location than at the CMP4 location. We attribute this discrepancy to
the uncertainty associated with the layer dating using Fe spikes (Fig. 5g) at the CMP3 location (section 4.3.1) by comparing
the CMP-derived SWE with SWE above the Fe peaks rather than considering the point mass balance observation (Fig. A5).
We discuss all uncertainties mentioned in this study in the following section.

565 6.5 Conservation of mass and uncertainties

Identification of CMP-derived IRHs as annual layers by chronologically comparing the CMP4-estimated SWE with point mass
balance-derived SWE (section 4.3) and firn core-based Fe peaks as summer horizon, and matching CMP3-derived SWE layers
to FC3-estimated SWE (section 4.3.1 and Fig. 5g) requires the assumption of conservation of mass. This means that between
2024 and 2025, no mass loss was observed, implying that the surface meltwater at the CMP4 location refroze within the same
570 layer. The same is also valid at the CMP3 location, where the surface melt is relatively low. This is supported by the estimated
SWE in the respective layers in 2024 and 2025, which match well ($R^2 > 0.9$; Fig. A2) at both locations. The comparison of
shallow firn cores from 2024 and 2025 (Fig. 6) indicates the validation of the conservation of mass assumption, as identified
ice lenses at ~6.25-6.5 m depth in 2024 are still seen in 2025, but at ~7-7.5 m. This indicates that, despite the 2024 summer
surface melt at the CMP2 location (similar elevation to CMP4 in Fig. 1), the meltwater refroze within the 2024 winter layer,
575 with no evidence of internal accumulation in subsequent layers. Further, ice core results from the Jungfraujoch drilled in 2002
illustrate that the subzero borehole temperatures (-4 and -6 °C) in the upper part of the firn zone, and high annual net accumu-
lation (1-2 m w.e), suggest the negligible percolation of melt through underlying annual layers (Schotterer and Stichler, 2002).
These limited direct observations support our mass-conservation assumption to some extent. However, our measurements do
not account for mass conservation during extreme melt seasons, such as the 2022 summer, due to the lack of data during those
580 periods.

Previous studies suggest that refreezing within the seasonal snowpack occurs when there is preferential flow through verti-
cal piping (Marsh and Woo, 1984; Albert et al., 1999; Evans et al., 2016; Williamson et al., 2020a). We hypothesise that
higher surface meltwater in extreme summers (e.g., summer 2022) percolates deeper and refreezes in the subsequent firn layer,
thereby altering the mass in the deeper layer through internal accumulation. These processes challenge our assumption of mass
585 conservation when meltwater drains from the glacier system. However, tracking meltwater percolation, preferential flow, and
refreezing complicates the understanding of firn, even though we can, to some extent, derive this information from deep firn
cores and CMP measurements. For this reason, we propose continuous monitoring of the Alpine firn using strain meters (Arth-



ern et al., 2010; MacFerrin et al., 2022), and radar techniques that are implemented to study polar firn, such as Autonomous Phase Sensitive Radar (ApRES), as stated in Nicholls et al. (2015); Case and Kingslake (2022).
590 Patil et al. (2025b) exemplifies uncertainties in V_{rms} picking from Semblance analysis, which increases with depth, and also illustrates challenges in picking IRHs that generate high permittivity contrast, such as ice lenses and visible Sahara dust layers. As explained by Booth et al. (2011), we assigned a sensitivity of 0.005 m ns^{-1} for the V_{rms} picking from the semblance analysis, which resulted in a density fluctuation of $60\text{-}100 \text{ kg m}^{-3}$. We observe that these uncertainties affect our density-depth profiles (Figs. 8, 9, and 11). As depth increases, the uncertainty in V_{rms} picking increases, and so does the density estimation.
595 Identifying the same IRH across multiple surveys is important, and any misidentification can amplify errors in compaction rates and annual layer depth estimates, as illustrated by Medley et al. (2015). The accuracy of picking IRHs from CMP gathers and identifying annual layers can contribute to significant uncertainties in temporal changes in firn density, compaction rate, and spatial accumulation estimation.

Furthermore, the thickness of identified layers is less sensitive to the V_{rms} pick than to the TWT pick. For instance, uncertainty
600 in 1 ns picking changes the neighbouring layer thickness by 10 cm. This uncertainty amplifies when the layers are thin and close to each other, impacting the compaction rate estimations (Fig. 10a). Additionally, it is reflected in the deeper layers, as shown in Figure 11, where the error bars are more pronounced with increasing depth (in layers 5-8). Similar uncertainties are discussed in Kruezmann et al. (2011), suggesting that bias in density measurements alters the TWT-to-depth estimations and emphasises density measurements as a potential source of error when deriving radar-wave velocities from firn-core-derived
605 density estimations. In our study, we assign potential sources of error to radar velocity and TWT picking, which govern the identification of IRHs as annual layers.

7 Conclusions

We have presented a novel geophysical approach using GPR-based CMP measurements to derive temporal changes in firn pack, such as firn density and compaction rate estimations at different parts of the Grosser Aletschgletscher's accumulation area. The
610 winter 2024 and 2025 multi-year CMP data, and GPR transects complemented by direct observations, such as firn cores, offer a unique dataset for firn studies. Our results demonstrate how firn properties are affected by processes such as surface melt, refreezing, and temperature lapse rate within the accumulation area of the Grosser Aletschgletscher. The comparison between firn density-depth profiles derived from direct (firn core) and indirect (CMP) observations at the same location correlates well, thus emphasising the suitability of the GPR-based CMP method as a complementary tool for the investigation of temporal
615 changes in firn pack. Our deep firn core-derived profiles of water-stable isotopes, chemical impurities, and visible Sahara dust layers provide independent validation to trace depth to the last summer horizon and date annual layers. Analysis of chemical impurities, particularly Fe, helps identify 10 annual layers by comparing the CMP-estimated SWE with the firn core from the upper part of the Ewigschneefeld. Furthermore, by applying a similar method introduced in previous studies (Sold et al., 2015; Patil et al., 2025b), we identified 10 annual layers at the Jungfraufirn location. The winter 2024 and 2025
620 CMP measurements at two locations of the accumulation area differ in elevations, which help quantify temporal and spatial



changes in firn density and compaction rates. The comparison of GPR transects gathered in two winter seasons offers better interpretation of firn stratigraphy, providing information on a possible new feature at the deeper depth (depth >25 m), which we speculate as a transition from temperate to cold glacier or influence of glacier dynamics. The 4.4 km-long GPR profile helped us trace the spatial extent of the firn body by locating the Equilibrium Line Altitude. We acknowledge limitations and 625 uncertainties that influence our results, mainly uncertainties associated with IRH picking from CMP semblance analysis, which are also addressed in Booth et al. (2011); Patil et al. (2025b). Our assumption of conservation of mass can be challenged if extreme summer melt drained from the glacier system rather than refreezing within the deeper layers (internal accumulation). Firn processes, such as meltwater percolation and refreezing, complicate the interpretation of indirect (GPR) measurements, even though multi-year CMP measurements offer quantification of temporal changes in firn pack, such as firn density and 630 compaction rate, but lack the detailed understanding of firn processes on a fine scale. We propose continuous monitoring of firn processes in Alpine glaciers through field observations, which will help calibrate existing firn models and improve glacier mass-balance estimates.



Appendix A: Accumulation history and spatial firn distribution

Figure A2a illustrates that CMP helped identify 11 annual firn layers among the more than 30 IRHs observed in the CMP2
635 radargram collected at the lower part of Ewigschneefeld. Similarly, 10 annual layers from the CMP4 (near the stake in Fig. 1) were obtained by following the method explained in section 4.3. Whereas, Figure A2b shows the identified 10 annual layers from the CMP3 measurement (upper part of Ewigschneefeld) are identified using Fe peaks from firn core chemical analysis (section 4.3.1). The total winter accumulation in 2025 (until the end of March) is estimated from point mass-balance measurements to be 1800 mm w.e., as shown by the blue vertical bar; the grey bars represent the annual accumulation for
640 each year. The seasonal and annual mass-balance measurements from long-term point measurements (Stake in Fig. 1) are demonstrated in Appendix Figure A1. It is noticeable that the extreme 2022 summer removed the entire winter accumulation and part of the 2021 firn layer (nearly 1000 mm w.e shown as cyan bar and CMP4) near the point mass-balance measurement site. However, this is not the case at the upper part of Ewigschneefeld (CMP3, Fig. A2b), which is evident from the radargram obtained from the GPR transect (Fig. 3) and shows that using CMP-derived density estimates, approximately 600 mm w.e of
645 the 2022 firn layer remained there. All CMP-derived SWE compared with the estimated SWE from the point mass-balance (grey bars) agrees well with R-square values, which are well above 0.9.

The spatial firn density and accumulation distribution can be estimated by tracing the annual layers on the radargram obtained from the GPR transect (Fig. 3b). Figure A3 demonstrates the firn density distribution between the upper CMP3 or FC3 (left) and lower CMP2 (right) gathered in winter 2025 at the Ewigschneefeld (Fig. 1 and Fig. 3b). It is observed that the winter
650 2025 layer has negligible variability in accumulated snow density, approximately 500 kg m^{-3} , at the two locations, which can be explained by the low winter temperatures during and after deposition. The annual layers below exhibit distinct density variations with increasing distance (left to right in Fig. A3). There exists a difference in density between the upper and lower ends of the profile, and we assume that density (linear) increases within each firn layer with distance. This illustrates that as the elevation decreases, firn density increases. The lower firn layers (2017 to 2015) show an increase in density from 700 to 750
655 kg m^{-3} and from 750 to 800 kg m^{-3} between the two CMP gathers. Further, the maximum density of around 760 kg m^{-3} is seen in 2016 and 2015 layers at 17-25 m depth at the upper part of the Ewigschneefeld, but the density of around 800 kg m^{-3} within the same layers can be observable near 10 m depth at the lower part of the Ewigschneefeld (distance > 1700 m).

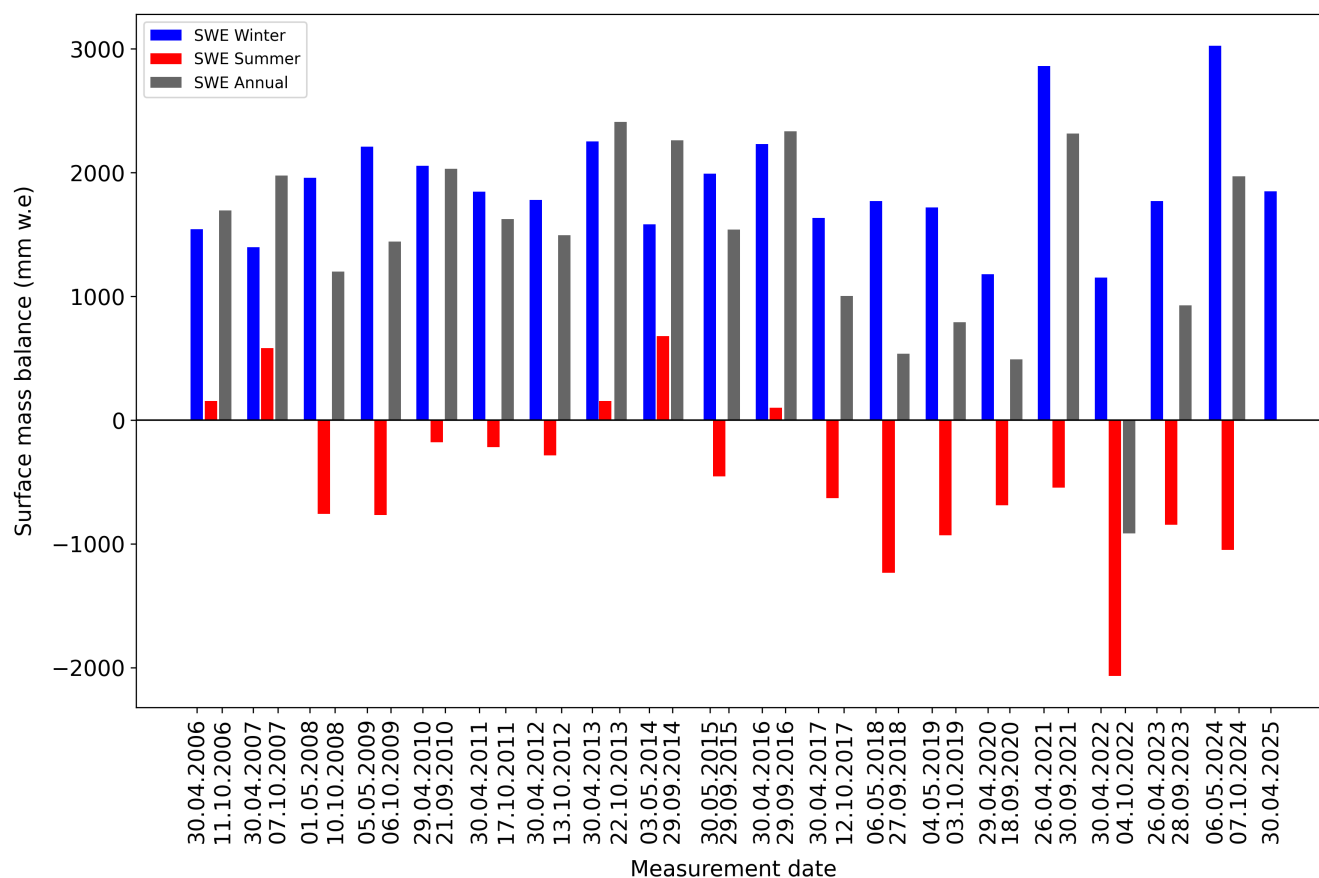


Figure A1. The long-term point mass balance measurements at the end of each season near the Jungfraufirn area (Fig. 1) of the Grosser Aletschgletscher glacier (approximate location: 46.54314 °N, 7.98389 °E, and elevation: 3340 m a.s.l.). The winter (blue) and summer (red) are the measured seasonal mass balance. The grey bars represent the annual balance estimated by adding the seasonal mass balance (winter and summer) over the last 20 years (GLAMOS (2025)). The seasonal mass balance measurement date is indicated on the x-axis.

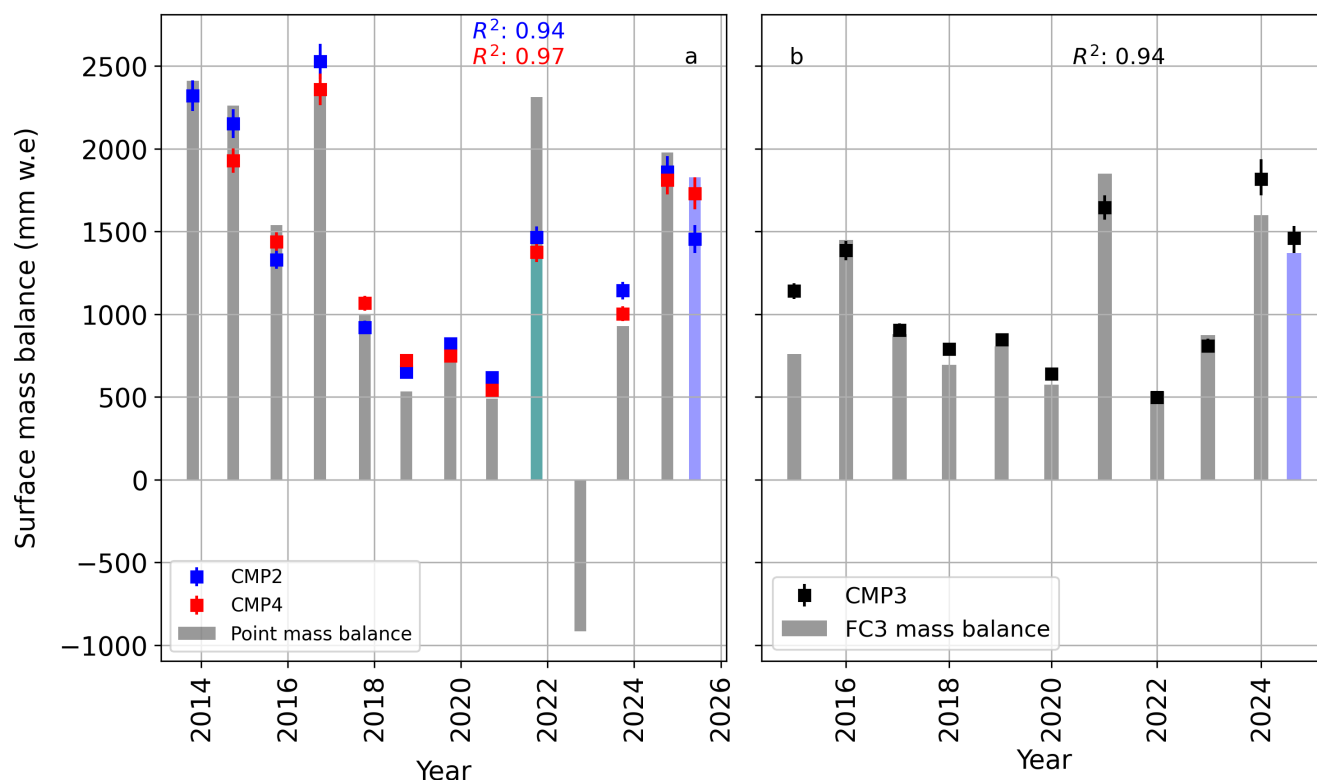


Figure A2. Identification of annual layers by comparing estimated SWE from three CMP gathers across the accumulation area of the Grosser Aletschgletscher with the measured SWE from point mass-balance measurements (Fig. 1). Blue squares represent the identified annual layers from the CMP2 (lower part of Ewigschneefeld, a), the red square, CMP4 near the point mass-balance measurement (Jungfrauirm), and the black square, CMP3 (upper part of Ewigschneefeld, b). The y-axis shows the annual surface mass balance in mm w.e, and the x-axis shows the year. The blue vertical bar shows the winter accumulation in 2025, and the cyan vertical bar in 2021 represents the remaining firn layer after the complete removal of the 2022 winter and some part of the 2021 layer (nearly 1000 mm w.e) at the point mass balance measurement location (Stake in Fig 1).

Similarly, the accumulation distribution across spatial scales is shown in Figure A4. The estimated accumulation is the
 660 product of the density gradient within the firn layers and the thickness of each picked layer. Thicker layers are visible at
 shallower depths, which correlates with high winter accumulation and/or relatively lower summer melt (Appendix Fig. A1).
 However, at lower elevations, the layer thickness reduces, particularly in years such as 2022, 2020, 2019, and 2018. The deeper
 layers (2016-2015) are well defined, with their thickness clearly visible throughout the radargram. The higher accumulation
 (>3000 mm w.e) in certain layers is directly associated with uncertainty in layer picking (subjective picking). The improved
 665 accuracy of the accumulation distribution relies on how well the IRHs can be picked. However, thinner, shallower layers
 (around 1000 and 2200 m along the profile and at 5-10 m depth) and deeper layers are visibly distinctive but difficult to pick
 accurately (Figs. 3a and b).

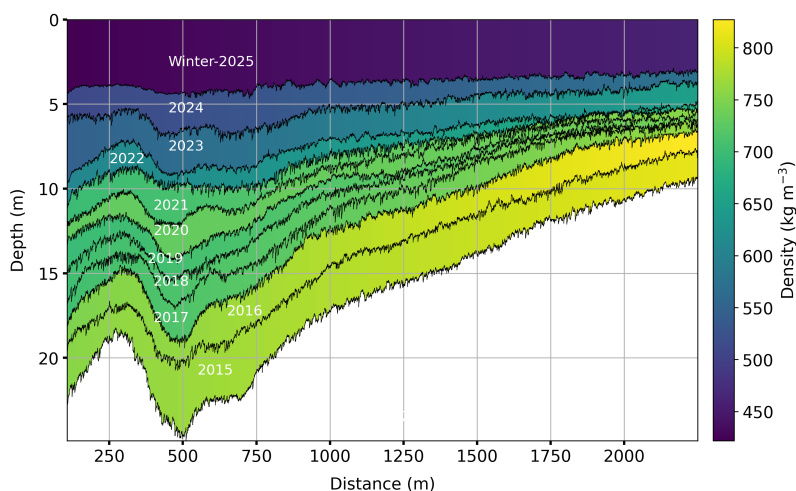


Figure A3. Illustration of the spatial firn density distribution estimated by interpolating the identified annual layer density using two CMP measurements gathered at the upper and lower parts of Ewigschneefeld near the GPR long transect (Fig. 1). The black wiggly lines are picked internal reflection horizons (IRHs) obtained from the GPR transect radargram, represented as annual layers marked with corresponding years in white.

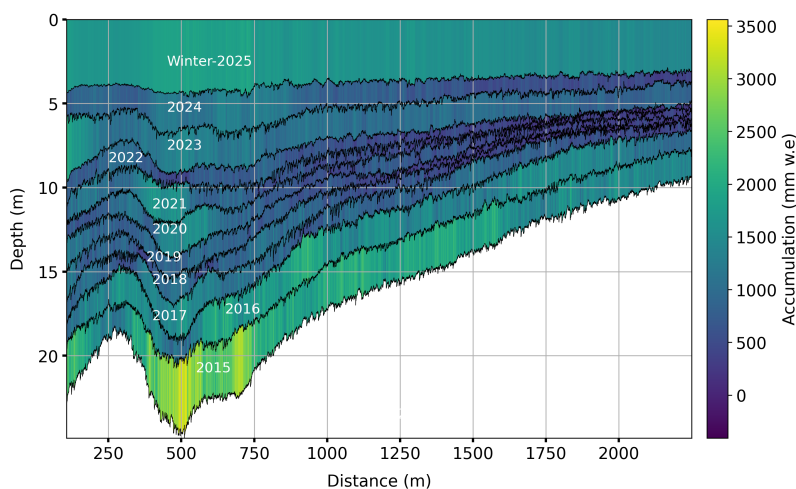


Figure A4. Illustration of the spatial accumulation distribution estimated by multiplying the interpolated annual layer density and the thickness using two CMP measurements gathered at the upper and lower parts of Ewigschneefeld near the GPR long transect (Fig. 1). The black wiggly lines are picked internal reflection horizons (IRHs) obtained from the GPR transect radargram, represented as annual layers marked with corresponding years in white.

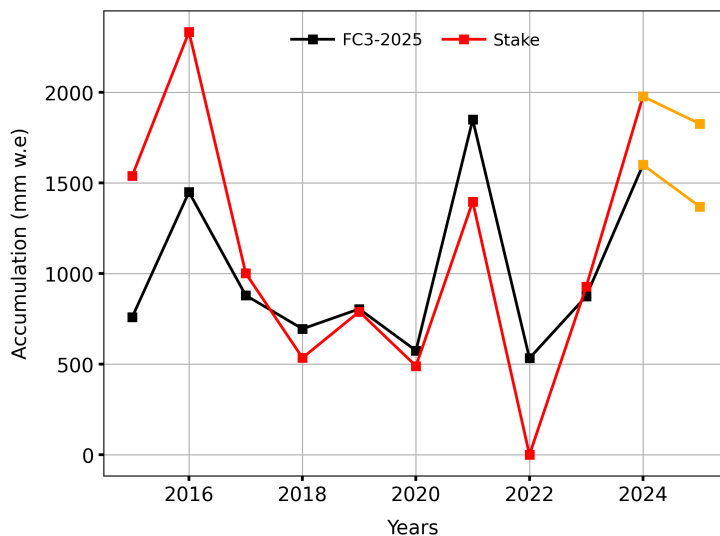


Figure A5. Comparison of accumulation within identified annual layers at the Upper part of Ewigschneefeld (black) using chemical impurity analysis (Fe) from deep firn core, and the point mass balance measurement near the stake (red) location (Jungfraufirn in Fig. 1). Orange lines show the winter accumulation at respective locations.

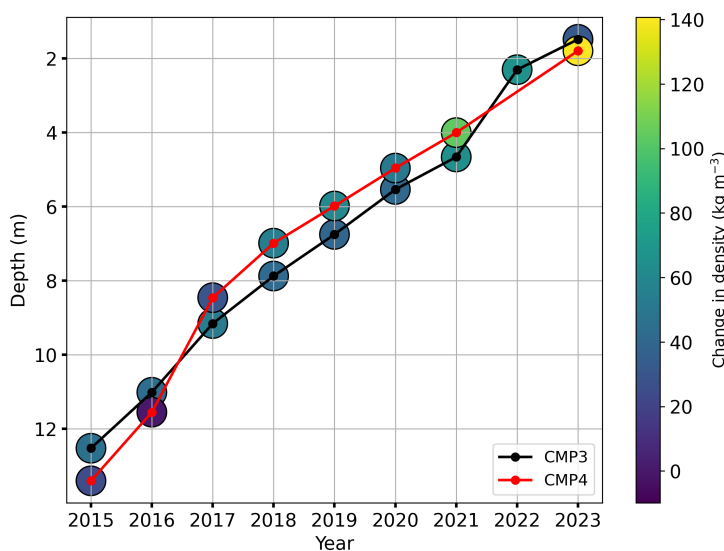


Figure A6. Illustration of changes in firm density with depth and age. The CMP3-derived (black line) and CMP4-estimated (red line) density changes at the upper part of the Ewigschneefeld and near the Stake (Fig. 1). The y-axis is the depth (m) of the identified annual layers, and the x-axis is the corresponding annual layers in years. The colour gradient represents density changes within the identified annual layers, and the corresponding density values are shown in the colour bar.



Data availability. The raw data acquired during the 2024-25 expedition are available on the BAdW LRZ online repository. We provide the data by establishing a repository with a DOI no later than the publication of the final reviewed manuscript as per the journal guidelines.
670 Already existing dataset that are used in this study are available at <https://doi.org/10.18750/massbalance.2025.r2025> (GLAMOS, 2025) and <https://doi.org/10.5281/zenodo.17077546> (Patil et al., 2025a).

Author contributions. AP with assistance from CM initiated and developed the study. AP. wrote the paper, conducted the data analysis, and performed all the visualisations. CM processed GPR long profile data. The field campaigns were planned with contributions from CM, TS, and AG. All co-authors contributed to the reviewing and editing of the manuscript.

675 *Competing interests.* The authors declare that they have no conflict of interest

Acknowledgements. The study was funded by the Bavarian State Ministry of Science and the Arts within the Elitenetwork Bavaria International Doctoral Programme “M3OCCA - Measuring and Modelling Mountain Glaciers and Ice Caps in a Changing Climate”. We thank Samuel Marending for his support during the 2025 field campaign. We also acknowledge the data provided by Dr. Andreas Bauder from ETH Zurich. We appreciate discussions with Dr. Carlos Martin from the British Antarctic Survey, Cambridge, UK. We also thank Dr. Christian Gerlach from BAdW, Munich, Germany, for his support with custom documentation. We also thank the International Foundation High
680 Alpine Research Stations Jungfraujoch and Gornergrat (HFSJG), and Jungfraubahn, Switzerland, for the smooth conduct of our expeditions.

Financial support. This research has been supported by the Elitenetzwerk Bayern (grant no. IDP M3OCCA) and the Deutsche Forschungsgemeinschaft (DFG) (grant number, SE 3091/5-1 awarded to Thorsten Seehaus). This research was further supported by Alexander R. Groos, who received primary funding from the European Union’s Horizon 2020 research and innovation programme via the European Research
685 Council (ERC) as a Starting Grant (FRAGILE project; principal investigator: Johannes J. Fürst) under grant agreement No. 948290.



References

- Albert, M., Koh, G., and Perron, F.: Radar investigations of melt pathways in a natural snowpack, *Hydrological Processes*, 13, 2991–3000, [https://doi.org/10.1002/\(SICI\)1099-1085\(19991230\)13:18<2991::AID-HYP10>3.0.CO;2-5](https://doi.org/10.1002/(SICI)1099-1085(19991230)13:18<2991::AID-HYP10>3.0.CO;2-5), 1999.
- Alean, J., Haeberli, W., and Schädler, B.: Snow accumulation, firn temperature and solar radiation in the area of the Colle Gnifetti core drilling site (Monte Rosa, Swiss Alps): distribution patterns and interrelationships, Tech. rep., 1983.
- 690 Ambach, W. and Eisner, H.: Analysis of a 20 m firn pit on the Kesselwandferner (Ötztal Alps), *Journal of Glaciology*, 6, 223–231, 1966.
- Annan, A. P.: Practical Processing of GPR Data, in: Proceedings of the Second Government Workshop on Ground Penetrating Radar, Columbus, Ohio, https://johnrleeman.com/documents/GPR_data_processing.pdf, 1993.
- Annan, A. P.: Ground-Penetrating Radar, in: Near-Surface Geophysics, pp. 357–438, Society of Exploration Geophysicists, 695 <https://doi.org/10.1190/1.9781560801719.ch11>, 2005.
- Arnaud, L., Barnola, J. M., and Duval, P.: Physical modeling of the densification of snow/firn and ice in the upper part of polar ice sheets, in: *Physics of Ice Core Records*, pp. 285–305, Hokkaido University Press, Hokkaido, Japan, 2000.
- Arthern, R. and Wingham, D.: The Natural Fluctuations of Firn Densification and Their Effect on the Geodetic Determination of Ice Sheet Mass Balance, *Climatic Change*, 40, 605–624, <https://doi.org/10.1023/A:1005320713306>, 1998.
- 700 Arthern, R. J., Vaughan, D. G., Rankin, A. M., Mulvaney, R., and Thomas, E. R.: In situ measurements of Antarctic snow compaction compared with predictions of models, *Journal of Geophysical Research: Earth Surface*, 115, 2009JF001306, <https://doi.org/10.1029/2009JF001306>, 2010.
- Avak, S. E., Schwikowski, M., and Eichler, A.: Impact and implications of meltwater percolation on trace element records observed in a high-Alpine ice core, *Journal of Glaciology*, 64, 877–886, <https://doi.org/10.1017/jog.2018.74>, 2018.
- 705 Avak, S. E., Trachsel, J. C., Edebeli, J., Brütsch, S., Bartels-Rausch, T., Schneebeli, M., Schwikowski, M., and Eichler, A.: Melt-Induced Fractionation of Major Ions and Trace Elements in an Alpine Snowpack, *Journal of Geophysical Research: Earth Surface*, 124, 1647–1657, <https://doi.org/https://doi.org/10.1029/2019JF005026>, 2019.
- Bader, H.: Sorge’s Law of Densification of Snow on High Polar Glaciers, *Journal of Glaciology*, 2, 319–323, <https://doi.org/10.3189/S0022143000025144>, 1954.
- 710 Bader, H.: Theory of densification of dry snow on high polar glaciers, II, Tech. Rep. 108, US Army Cold Regions Research and Engineering Laboratory, 1962.
- Bannwart, J., Piermattei, L., Dussaillant, I., Krieger, L., Floricioiu, D., Berthier, E., Roeoesli, C., Machguth, H., and Zemp, M.: Elevation bias due to penetration of spaceborne radar signal on Grosser Aletschgletscher, Switzerland, *Journal of Glaciology*, 70, e1, <https://doi.org/10.1017/jog.2024.37>, 2024.
- 715 Benson, C. S.: Stratigraphic Studies in the Snow and Firn of the Greenland Ice Sheet, Tech. Rep. Technical Report 70, U.S. Army Snow, Ice and Permafrost Research Establishment (SIPRE), <https://apps.dtic.mil/sti/citations/ADA337542>, 1962.
- Bezeau, P., Sharp, M., Burgess, D., and Gascon, G.: Firn profile changes in response to extreme 21st-century melting at Devon Ice Cap, Nunavut, Canada, *Journal of Glaciology*, 59, 981–991, <https://doi.org/10.3189/2013JOG12J208>, 2013.
- Blatter, H. and Hutter, K.: Polythermal conditions in Arctic glaciers, *Journal of Glaciology*, 37, 261–269, 1991.
- 720 Booth, A. D., Clark, R. A., and Murray, T.: Influences on the resolution of GPR velocity analyses and a Monte Carlo simulation for establishing velocity precision, *Near Surface Geophysics*, 9, 399–411, <https://doi.org/10.3997/1873-0604.2011019>, 2011.



- Braithwaite, R. J., Laternser, M., and Pfeffer, W. T.: Variations of near-surface firn density in the lower accumulation area of the Greenland ice sheet, Pákitsoq, West Greenland, *Journal of Glaciology*, 40, 477–485, 1994.
- Case, E. and Kingslake, J.: Phase-sensitive radar as a tool for measuring firn compaction, *Journal of Glaciology*, 68, 139–152, <https://doi.org/10.1017/jog.2021.83>, 2022.
- 725 Clifford, H. M., Spaulding, N. E., Kurbatov, A. V., More, A., Korotkikh, E. V., Sneed, S. B., et al.: A 2000 year Saharan dust event proxy record from an ice core in the European Alps, *Journal of Geophysical Research: Atmospheres*, 124, 12 882–12 900, <https://doi.org/10.1029/2019JD030725>, 2019.
- Cogley, J. G., Hock, R., Rasmussen, L. A., Arendt, A. A., Bauder, A., Braithwaite, R. J., Jansson, P., Kaser, G., Möller, M., Nicholson, L., and Zemp, M.: Glossary of Glacier Mass Balance and Related Terms, no. 86 in IHP-VII Technical Documents in Hydrology, UNESCO-IHP, Paris, iACS Contribution No. 2, 2011.
- 730 Colbeck, S. C.: The difficulties of measuring the water saturation and porosity of snow, *Journal of Glaciology*, 20, 189–201, <https://doi.org/10.3189/S0022143000198089>, 1978.
- Cuffey, K. M. and Paterson, W. S. B.: *The Physics of Glaciers*, Butterworth-Heinemann, Oxford, 4 edn., ISBN 978-0-12-369461-4, https://booksite.elsevier.com/samplechapters/9780123694614/01~Front_Matter.pdf, last access: 21 October 2025, 2010.
- 735 Davis, J. L. and Annan, A. P.: GROUND-PENETRATING RADAR FOR HIGH-RESOLUTION MAPPING OF SOIL AND ROCK STRATIGRAPHY¹, *Geophysical Prospecting*, 37, 531–551, <https://doi.org/10.1111/j.1365-2478.1989.tb02221.x>, 1989.
- Eichler, A., Legrand, M., Jenk, T. M., Preunkert, S., Andersson, C., Eckhardt, S., et al.: Consistent histories of anthropogenic western European air pollution preserved in different Alpine ice cores, *The Cryosphere*, 17, 2119–2137, <https://doi.org/10.5194/tc-17-2119-2023>, 2023.
- 740 Endres, A. L., Murray, T., Booth, A. D., and West, L. J.: A new framework for estimating englacial water content and pore geometry using combined radar and seismic wave velocities, *Geophysical Research Letters*, 36, 2008GL036 876, <https://doi.org/10.1029/2008GL036876>, 2009.
- Evans, S. L., Flores, A. N., Heilig, A., Kohn, M. J., Marshall, H. P., and McNamara, J. P.: Isotopic evidence for lateral flow and diffusive transport, but not sublimation, in a sloped seasonal snowpack, Idaho, USA, *Geophysical Research Letters*, 43, 3298–3306, <https://doi.org/10.1002/2015GL067605>, 2016.
- 745 Fisher, D. A., Wake, C., Kreutz, K., Yalcin, K., Steig, E., Mayewski, P., Anderson, L., Zheng, J., Rupper, S., Zdanowicz, C., Demuth, M., Waszkiewicz, M., Dahl-Jensen, D., Goto-Azuma, K., Bourgeois, J. B., Koerner, R. M., Sekerka, J., Osterberg, E., Abbott, M. B., Finney, B. P., and Burns, S. J.: Stable Isotope Records from Mount Logan, Eclipse Ice Cores and Nearby Jellybean Lake. Water Cycle of the North Pacific Over 2000 Years and Over Five Vertical Kilometres: Sudden Shifts and Tropical Connections, *Géographie physique et Quaternaire*, 58, 337–352, <https://doi.org/10.7202/013147ar>, 2006.
- 750 Fisher, S. C., Stewart, R. R., and Jol, H. M.: Ground Penetrating Radar (GPR) Data Enhancement Using Seismic Techniques, *Journal of Environmental & Engineering Geophysics*, 1, 89–96, <https://doi.org/10.4133/JEEG1.2.89>, 1996.
- Fountain, A. G. and Walder, J. S.: Water flow through temperate glaciers, *Reviews of Geophysics*, 36, 299–328, 1998.
- 755 Fujita, S., Hirabayashi, M., Goto-Azuma, K., Dallmayr, R., Satow, K., Zheng, J., and Dahl-Jensen, D.: Densification of layered firn of the ice sheet at NEEM, Greenland, *Journal of Glaciology*, 60, 905–921, <https://doi.org/10.3189/2014JoG14J006>, 2014.
- Gerland, S., Oerter, H., Kipfstuhl, J., Wilhelms, F., Miller, H., and Miners, W. D.: Density log of a 181 m long ice core from Berkner Island, Antarctica, *Annals of Glaciology*, 29, 215–219, 1999.



- Gillet-Chaulet, F., Hindmarsh, R. C. A., Corr, H. F. J., King, E. C., and Jenkins, A.: In-situ quantification of ice rheology and direct measurement of the Raymond Effect at Summit, Greenland using a phase-sensitive radar, *Geophysical Research Letters*, 38, L24503, <https://doi.org/10.1029/2011GL049843>, 2011.
- Ginot, P., Stampfli, F., Stampfli, D., Schwikowski, M., and Gäggeler, H. W.: FELICS, a new ice core drilling system for high-altitude glaciers, *Memoirs of National Institute of Polar Research: Special Issue*, 56, 38–48, 2002.
- GLAMOS: The Swiss Glaciers 2015/16 and 2016/17, Tech. Rep. Glaciological Report No. 135/136, Cryospheric Commission (EKK) of the Swiss Academy of Sciences (SCNAT), https://doi.org/10.18752/glrp_137-138, under review; 126 pages, 2018a.
- GLAMOS: The Swiss Glaciers 1880-2016/17, Glaciological Reports No 1-140, Yearbooks of the Cryospheric Commission of the Swiss Academy of Sciences (SCNAT), Zurich, https://doi.org/10.18752/glrep_series, since 1964 by VAW / ETH Zurich, ed., 2018b.
- GLAMOS: The Swiss Glaciers 2019/20 and 2020/21, Tech. Rep. Glaciological Report No. 141/42, Cryospheric Commission (EKK) of the Swiss Academy of Sciences (SCNAT), https://doi.org/10.18752/glrep_141-142, 2022.
- GLAMOS: Swiss Glacier Mass Balance, release 2025, <https://doi.org/10.18750/massbalance.2025.r2025>, 2025.
- Grab, M., Mattea, E., Bauder, A., et al.: Ice thickness distribution of all Swiss glaciers based on extended ground-penetrating radar data and glaciological modeling, *Journal of Glaciology*, 67, 1074–1092, <https://doi.org/10.1017/jog.2021.55>, 2021.
- Haeberli, W. and Alean, J.: Temperature and accumulation of high altitude firn in the Alps, *Annals of Glaciology*, 6, 161–163, 1985.
- Hamilton, G. S., Whillans, I. M., and Morgan, P. J.: First point measurements of ice-sheet thickness change in Antarctica, *Annals of Glaciology*, 27, 125–129, <https://doi.org/10.3189/1998AoG27-1-125-129>, 1998.
- Hawley, R. L. and Waddington, E. D.: In situ measurements of firn compaction profiles using borehole optical stratigraphy, *Journal of Glaciology*, 57, 289–294, <https://doi.org/10.3189/002214311796405889>, 2011.
- Hawley, R. L., Waddington, E. D., Lamorey, G. W., and Taylor, K. C.: Vertical-strain measurements in firn at Siple Dome, Antarctica, *Journal of Glaciology*, 50, 447–452, <https://doi.org/10.3189/172756504781829972>, 2004.
- Herron, M. M. and Langway, C. C.: Firn Densification: An Empirical Model, *Journal of Glaciology*, 25, 373–385, <https://doi.org/10.3189/S0022143000015239>, 1980.
- Hooke, R. L., Gould, J. E., and Brzozowski, J.: Near-surface temperatures near and below the equilibrium line on polar and subpolar glaciers, *Zeitschrift für Gletscherkunde und Glazialgeologie*, 19, 1–25, 1983.
- Horlings, A. N., Christianson, K., and Miège, C.: Expansion of Firn Aquifers in Southeast Greenland, *Journal of Geophysical Research: Earth Surface*, 127, e2022JF006753, <https://doi.org/10.1029/2022JF006753>, 2022.
- Hubbard, B., Philippe, M., Pattyn, F., Drews, R., Young, T. J., Bruyninx, C., Bergeot, N., Fjøsne, K., and Tison, J.-L.: High-resolution distributed vertical strain and velocity from repeat borehole logging by optical televiewer: Derwael Ice Rise, Antarctica, *Journal of Glaciology*, 66, 523–529, <https://doi.org/10.1017/jog.2020.18>, 2020.
- Huber, C. J., Eichler, A., Mattea, E., Brütsch, S., Jenk, T. M., Gabrieli, J., Barbante, C., and Schwikowski, M.: High-altitude glacier archives lost due to climate change-related melting, *Nature Geoscience*, 17, 110–113, <https://doi.org/10.1038/s41561-023-01366-1>, 2024.
- Huss, M.: Density assumptions for converting geodetic glacier volume change to mass change, *The Cryosphere*, 7, 877–887, <https://doi.org/10.5194/tc-7-877-2013>, 2013.
- Huss, M., Bauder, A., and Funk, M.: Homogenization of long-term mass balance time series, *Annals of Glaciology*, 50, 198–206, 2009.
- icedrill.ch AG.: IceDrill.ch, <http://icedrill.ch>, accessed: 24 March 2026, 2010.
- Kawashima, K. and Yamada, T.: Experimental studies on the transformation from firn to ice in the wet-snow zone of temperate glaciers, *Annals of Glaciology*, 24, 181–185, <https://doi.org/10.3189/S0260305500012143>, 1997.



- Kindstedt, I., Winski, D., Stevens, C. M., Skelton, E., Copland, L., Kreutz, K., Mannello, M., Clavette, R., Holmes, J., Albert, M., and Williamson, S. N.: Ongoing firn warming at Eclipse Icefield, Yukon, indicates potential widespread meltwater percolation and retention in firn pack across the St. Elias Range, *The Cryosphere*, 19, 3655–3680, <https://doi.org/10.5194/tc-19-3655-2025>, 2025.
- 800 Kingslake, J. et al.: Full-depth englacial vertical ice sheet velocities measured using phase-sensitive radar, *Journal of Geophysical Research: Earth Surface*, 119, 2014JF003 275, <https://doi.org/10.1002/2014JF003275>, 2014.
- Knight, R., Tercier, P., and Irving, J.: The effect of vertical measurement resolution on the correlation structure of a ground penetrating radar reflection image, *Geophysical Research Letters*, 31, 2004GL021 112, <https://doi.org/10.1029/2004GL021112>, 2004.
- Kruetzmann, N. C., Rack, W., McDonald, A. J., and George, S. E.: Snow accumulation and compaction derived from GPR data near Ross 805 Island, Antarctica, *The Cryosphere*, 5, 391–404, <https://doi.org/10.5194/tc-5-391-2011>, 2011.
- Lang, H.: Is evaporation an important component in high Alpine hydrology?, *Nordic Hydrology*, 12, 217–224, 1981.
- Leinss, S. and Bernhard, P.: TanDEM-X: Deriving InSAR Height Changes and Velocity Dynamics of Great Aletsch Glacier, *IEEE Journal of Selected Topics in Applied Earth Observations and Remote Sensing*, PP, 1–1, <https://doi.org/10.1109/JSTARS.2021.3078084>, 2021.
- Li, J. and Zwally, H. J.: Modeling the density variation in the shallow firn layer, *Annals of Glaciology*, 38, 309–313, 810 <https://doi.org/10.3189/172756404781814988>, 2004.
- Ligtenberg, S. R. M., Helsen, M. M., and Van Den Broeke, M. R.: An improved semi-empirical model for the densification of Antarctic firn, *The Cryosphere*, 5, 809–819, <https://doi.org/10.5194/tc-5-809-2011>, 2011.
- Linsbauer, A., Huss, M., Hodel, E., Bauder, A., Fischer, M., Weidmann, Y., Bärtschi, H., and Schmassmann, E.: The New Swiss Glacier Inventory SGI2016: From a Topographical to a Glaciological Dataset, *Frontiers in Earth Science*, 9, 704 189, 815 <https://doi.org/10.3389/feart.2021.704189>, 2021.
- Looyenga, H.: Dielectric constants of heterogeneous mixtures, *Physica*, 31, 401–406, [https://doi.org/10.1016/0031-8914\(65\)90045-5](https://doi.org/10.1016/0031-8914(65)90045-5), 1965.
- Lüthi, M. and Funk, M.: Dating ice cores from a high Alpine glacier with a flow model for cold firn, *Annals of Glaciology*, 31, 69–79, 2000.
- MacFerrin, M. J., Stevens, C. M., Vandecrux, B., Waddington, E. D., and Abdalati, W.: The Greenland Firn Compaction Verification and Reconnaissance (FirnCover) dataset, 2013–2019, *Earth System Science Data*, 14, 955–971, <https://doi.org/10.5194/essd-14-955-2022>, 820 2022.
- Maeno, N. and Ebinuma, T.: Pressure sintering of ice and its implication to the densification of snow at polar glaciers and ice sheets, *Journal of Physical Chemistry*, 87, 4103–4110, 1983.
- Marsh, P. and Woo, M.-K.: Wetting front advance and freezing of meltwater within a snow cover: I. Observations in the Canadian Arctic, *Water Resources Research*, 20, 1853–1864, <https://doi.org/10.1029/WR020i012p01853>, 1984.
- 825 McMillan, M., Leeson, A., Shepherd, A., Briggs, K., Armitage, T. W. K., Hogg, A., Kuipers Munneke, P., van den Broeke, M., Noël, B., van de Berg, W. J., Ligtenberg, S., Horwath, M., Groh, A., Muir, A., and Gilbert, L.: A high-resolution record of Greenland mass balance, *Geophysical Research Letters*, 43, 7002–7010, <https://doi.org/10.1002/2016GL069666>, 2016.
- Medley, B., Ligtenberg, S., Joughin, I., Van Den Broeke, M., Gogineni, S., and Nowicki, S.: Antarctic firn compaction rates from repeat-track airborne radar data: I. Methods, *Annals of Glaciology*, 56, 155–166, <https://doi.org/10.3189/2015AoG70A203>, 2015.
- 830 MeteoSchweiz: Jahresverlauf an Stationen. Jungfrauoch, <https://www.meteoswiss.admin.ch/services-and-publications/applications/measurement-values-and-measuring-networks.html#param=messnetz-automatisch&lang=en&station=JUN&chart=day&table=false&compare=n>, accessed: 2026-02-06, 2025.
- Miller, J. B., Frisbee, M. D., Hamilton, T. L., and Murugapiran, S. K.: Recharge from glacial meltwater is critical for alpine springs and their microbiomes, *Environmental Research Letters*, 16, 064 012, <https://doi.org/10.1088/1748-9326/abf06b>, 2021.



- 835 Morris, E. M. and Wingham, D. J.: Densification of polar snow: Measurements, modeling, and implications for altimetry, *Journal of Geophysical Research: Earth Surface*, 119, 349–365, <https://doi.org/10.1002/2013JF002898>, 2014.
- Nicholls, K. W., Corr, H. F., Stewart, C. L., Lok, L. B., Brennan, P. V., and Vaughan, D. G.: A ground-based radar for measuring vertical strain rates and time-varying basal melt rates in ice sheets and shelves, *Journal of Glaciology*, 61, 1079–1087, <https://doi.org/10.3189/2015JoG15J073>, 2015.
- 840 Ochwat, N. E., Marshall, S. J., Moorman, B. J., Criscitiello, A. S., and Copland, L.: Evolution of the firn pack of Kaskawulsh Glacier, Yukon: meltwater effects, densification, and the development of a perennial firn aquifer, *The Cryosphere*, 15, 2021–2040, <https://doi.org/10.5194/tc-15-2021-2021>, 2021.
- Oeschger, H., Schotterer, U., Stauffer, B., Haerberli, W., and Röhrlisberger, H.: First results from Alpine core drilling projects, *Zeitschrift für Gletscherkunde und Glazialgeologie*, 13, 193–208, heft 1/2, 1977.
- 845 Patil, A., Mayer, C., Seehaus, T., Groos, A. R., Lambrecht, A., Pfluger, F., Schlenk, P., Saigger, M., and Stelzig, M.: Ground Penetrating Radar and Glaciological methods: Firn structure and density measurements in the accumulation area of the Grosser Aletschgletscher winter-2024, <https://doi.org/10.5281/zenodo.17077546>, 2025a.
- Patil, A. M., Mayer, C., Seehaus, T., Groos, A. R., and Bauder, A.: Investigating firn structure and density in the accumulation area of the Grosser Aletschgletscher using ground-penetrating radar, *The Cryosphere*, 19, 5547–5577, <https://doi.org/10.5194/tc-19-5547-2025>,
850 2025b.
- Pfeffer, W. T. and Humphrey, N. F.: Determination of timing and location of water movement and ice-layer formation by temperature measurements in sub-freezing snow, *Journal of Glaciology*, 42, 292–304, <https://doi.org/10.3189/S0022143000004159>, 1996.
- Reeh, N.: A nonsteady-state firn-densification model for the percolation zone of a glacier, *Journal of Geophysical Research*, 113, F03 023, <https://doi.org/10.1029/2007JF000746>, 2008.
- 855 Rückamp, M., Cheng, G., Gutjahr, K., Möller, M., Pellikka, P. K. E., and Mayer, C.: Future Retreat of Great Aletsch Glacier and Hintereisferner – application of a full-Stokes model to two valley glaciers in the European Alps, *EGUsphere*, <https://doi.org/10.5194/egusphere-2025-3150>, preprint, 2025.
- Samimi, S. and Marshall, S. J.: Diurnal Cycles of Meltwater Percolation, Refreezing, and Drainage in the Supraglacial Snowpack of Haig Glacier, Canadian Rocky Mountains, *Frontiers in Earth Science*, 5, <https://doi.org/10.3389/feart.2017.00006>, 2017.
- 860 Sandmeier, K.: Reflex-Win Version 5.5.1, Sandmeier Scientific Software, <https://www.sandmeier-geo.de/reflexw.html>, ground penetrating radar data processing software, 2010.
- Schmelzbach, C., Tronicke, J., and Dietrich, P.: High-resolution water content estimation from surface-based ground-penetrating radar reflection data by impedance inversion, *Water Resources Research*, 48, 2012WR011 955, <https://doi.org/10.1029/2012WR011955>, 2012.
- Schneider, T. and Jansson, P.: Internal accumulation in firn and its significance for the mass balance of Storglaciären, Sweden, *Journal of Glaciology*, 50, 25–34, <https://doi.org/10.3189/172756504781830277>, 2004.
- 865 Schotterer, U. and Stichler, W.: Extending isotope in precipitation data beyond direct measurements: the perspective from glacier ice-core measurements in Switzerland, in: *Stable Isotopes*, edited by Edwards, T. D., Kull, C., and Alverson, K., vol. 10-2 of *PAGES News*, pp. 6–7, 2002.
- Schotterer, U., Finkel, R., Oeschger, H., Siegenthaler, U., Wahlen, M., Bart, G., and von Gunten, H. R.: Isotope measurements on firn and
870 ice cores from Alpine glaciers, in: *Isotopes and Impurities in Snow and Ice*, vol. 118 of *IAHS Publication*, pp. 232–236, 1977.



- Schotterer, U., Stichler, W., and Ginot, P.: The influence of post-depositional effects on ice core studies: examples from the Alps, Andes, and Altai, in: *Earth Paleoenvironments: Records Preserved in Mid- and Low-Latitude Glaciers*, edited by Green, J. R. and Thompson, L. G., vol. 9 of *Developments in Paleoenvironmental Research*, Springer, Dordrecht, https://doi.org/10.1007/1-4020-2146-1_3, 2004.
- Schwarb, M., Daly, C., Frei, C., and Schär, C.: Mean annual and seasonal precipitation in the European Alps 1971–1990, in: *Hydrological Atlas of Switzerland*, Federal Office for the Environment (FOEN), Bern, Switzerland, 2001.
- Schwikowski, M., Brütsch, S., Gäggeler, H. W., and Schotterer, U.: A high-resolution air chemistry record from an Alpine ice core: Fiescherhorn Glacier, Swiss Alps, *Journal of Geophysical Research: Atmospheres*, 104, 13 709–13 719, <https://doi.org/10.1029/1998JD100112>, 1999.
- Shapiro, L. H., Johnson, J. B., Sturm, M., and Blaisdell, G. L.: *Snow Mechanics: Review of the State of Knowledge and Applications*, Tech. rep., Defense Technical Information Center, Fort Belvoir, VA, <https://doi.org/10.21236/ADA330695>, 1997.
- Shepherd, A., Ivins, E. R., A. G., Barletta, V. R., Bentley, M. J., Bettadpur, S., Briggs, K. H., Bromwich, D. H., Forsberg, R., Galin, N., Horwath, M., Jacobs, S., Joughin, I., King, M. A., Lenaerts, J. T. M., Li, J., Ligtenberg, S. R. M., Luckman, A., Luthcke, S. B., McMillan, M., Meister, R., Milne, G., Mouginot, J., Muir, A., Nicolas, J. P., Paden, J., Payne, A. J., Pritchard, H., Rignot, E., Rott, H., Sørensen, L. S., Scambos, T. A., Scheuchl, B., Schrama, E. J. O., Smith, B., Sundal, A. V., Van Angelen, J. H., Van De Berg, W. J., Van Den Broeke, M. R., Vaughan, D. G., Velicogna, I., Wahr, J., Whitehouse, P. L., Wingham, D. J., Yi, D., Young, D., and Zwally, H. J.: A Reconciled Estimate of Ice-Sheet Mass Balance, *Science*, 338, 1183–1189, <https://doi.org/10.1126/science.1228102>, 2012.
- Sheriff, R. E. and Geldart, L. P.: *Exploration Seismology*, Cambridge University Press, 2 edn., ISBN 0-521-46282-7, 1999.
- Simonsen, S. B., Stenseng, L., Aðalgeirsdóttir, G., Fausto, R. S., Hvidberg, C. S., and Lucas-Picher, P.: Assessing a multilayered dynamic firn-compaction model for Greenland with ASIRAS radar measurements, *Journal of Glaciology*, 59, 545–558, <https://doi.org/10.3189/2013JoG12J158>, 2013.
- Smith, B. et al.: Pervasive ice sheet mass loss reflects competing ocean and atmosphere processes, *Science*, 368, 1239–1242, <https://doi.org/10.1126/science.aaz5845>, 2020.
- Sold, L., Huss, M., Eichler, A., Schwikowski, M., and Hoelzle, M.: Unlocking annual firn layer water equivalents from ground-penetrating radar data on an Alpine glacier, *The Cryosphere*, 9, 1075–1087, <https://doi.org/10.5194/tc-9-1075-2015>, 2015.
- Stevens, C. M., Sass, L., Florentine, C., McNeil, C., Baker, E., and Bollen, K.: Direct measurements of firn-density evolution from 2016 to 2022 at Wolverine Glacier, Alaska, *Journal of Glaciology*, 70, e2, <https://doi.org/10.1017/jog.2024.24>, 2024.
- Suter, S., Laternser, M., Haeberli, W., Frauenfelder, R., and Hoelzle, M.: Cold firn and ice of high-altitude glaciers in the Alps: Measurements and distribution modelling, *Journal of Glaciology*, 47, 85–96, 2001.
- Topp, G. C., Davis, J. L., and Annan, A. P.: Electromagnetic determination of soil water content: Measurements in coaxial transmission lines, *Water Resources Research*, 16, 574–582, <https://doi.org/10.1029/WR016i003p00574>, 1980.
- Ulriksen, C. P.: *Application of Impulse Radar to Civil Engineering*, Ph.D. thesis, Lund University of Technology, Lund, Sweden, <http://www.nypl.org/research/research-catalog/bib/pb9910011683506421>, 1982.
- van den Broeke, M., van de Berg, W. J., and van Meijgaard, E.: Firn depth correction along the Antarctic grounding line, *Antarctic Science*, 20, 513–517, <https://doi.org/10.1017/S095410200800148X>, 2008.
- Vandecrux, B., Mottram, R., Langen, P. L., Fausto, R. S., Olesen, M., Stevens, C. M., Verjans, V., Leeson, A., Ligtenberg, S., Kuipers Munneke, P., Marchenko, S., van Pelt, W., Meyer, C. R., Simonsen, S. B., Heilig, A., Samimi, S., Marshall, S., Machguth, H., MacFerrin, M., Niwano, M., Miller, O., Voss, C. I., and Box, J. E.: The firn meltwater Retention Model Intercomparison Project



(RetMIP): evaluation of nine firn models at four weather station sites on the Greenland ice sheet, *The Cryosphere*, 14, 3785–3810, <https://doi.org/10.5194/tc-14-3785-2020>, 2020.

910 Vandecrux, B. et al.: Firn data compilation reveals widespread decrease of firn air content in western Greenland, *The Cryosphere*, 13, 845–859, <https://doi.org/10.5194/tc-13-845-2019>, 2019.

Wharton, R. P., Hazen, G. A., Rau, R. N., and Best, D. L.: Electromagnetic Propagation Logging: Advances in Technique and Interpretation, in: *SPE Annual Technical Conference and Exhibition*, SPE Paper 9267, Society of Petroleum Engineers, Dallas, Texas, <https://doi.org/10.2118/9267-MS>, 1980.

915 Williamson, S. N., Zdanowicz, C., Anslow, F. S., Clarke, G. K. C., Copland, L., Danby, R. K., Flowers, G. E., Holdsworth, G., Jarosch, A. H., and Hik, D. S.: Evidence for elevation dependent warming in the St. Elias Mountains, Yukon, Canada, *Journal of Climate*, 33, 3253–3269, <https://doi.org/10.1175/JCLI-D-19-0405.1>, 2020a.

Williamson, S. N., Zdanowicz, C., Anslow, F. S., Clarke, G. K. C., Copland, L., Danby, R. K., Flowers, G. E., Holdsworth, G., Jarosch, A. H., and Hik, D. S.: Evidence for Elevation-Dependent Warming in the St. Elias Mountains, Yukon, Canada, *Journal of Climate*, 33, 3253–3269, <https://doi.org/10.1175/JCLI-D-19-0405.1>, 2020b.

920 Yilmaz, : *Seismic Data Analysis: Processing, Inversion, and Interpretation of Seismic Data*, Society of Exploration Geophysicists, ISBN 978-1-56080-094-1 978-1-56080-158-0, <https://doi.org/10.1190/1.9781560801580>, 2001.

Zwally, H. J. et al.: Greenland ice sheet mass balance: distribution of increased mass loss with climate warming, *Journal of Glaciology*, 57, 88–102, 2011.